LUND UNIVERSITY
Faculty of Science

X-Ray Resonant Magnetic Scattering Studies of the $j_{\mathrm{eff}} = 1/2$ State in Epitaxial Sr_2IrO_4 Thin Films

Björn Erik Skovdal

Thesis submitted for the degree of master of science
Project duration: 12 months

Supervised by Dan Mannix and Anders Mikkelsen

Department of Physics
Division of Synchrotron Radiation Research
January 2016

Abstract

Transition metal oxides of $5d$ elements have been subject to close investigation in recent years. These compounds display interesting physical properties emerging from their exceptionally large energy parameter space. Epitaxial thin films of one such compound, namely the layered perovskite Sr_2IrO_4, has been thoroughly studied in this thesis. X-ray resonant magnetic scattering at the L_3 edge was used to probe the novel $j_{\text{eff}} = 1/2$ ground state in order to determine the magnetic structure. The samples were then studied under the influence of magnetic fields and temperature. The determined magnetic structure was to a large extent similar to bulk Sr_2IrO_4, with an apparent difference in dimensionality. The samples investigated in this theses behaved like 3D magnets while bulk samples have previously been found to show 2D-like behaviour. A novel temperature dependent hysteresis effect was observed that is possibly related to strain effects exerted by a $SrTiO_3$ substrate.

Acknowledgments

First, I would like to express sincere gratitude to my supervisor Dan Mannix for devotedly guiding me along this project by hours of consultation. I appreciate you challenging my understanding and pushing my interest forward. I should not forget to mention how much I enjoyed our two trips to France where I got the full experience of scientific research and the beautiful city of Grenoble.

I should also thank my other supervisor Anders Mikkelsen for helping me to find this project.

I must thank Stephan Geprägs for growing the samples that were investigated and for the collaboration at the beamline. I also thank you for providing me with some nice figures to include in this thesis.

Lastly, I must acknowledge the XMaS beamline staff, Paul Thompson and Didier Wermeille for the immense assistance with the experiments. Also, thank you Paul, Dan and Stephan for all the beer you bought me in the pub.

Acronyms

AFM Antiferromagnetic. 13

DOS Density of States. 28

FM Ferromagnetic. 13

MBE Molecular Beam Epitaxy. 15, 16

PLD Pulsed Laser Deposition. 16, 17

RHEED Reflection High-Energy Electron Diffraction. 16, 17

SIO Strontium Iridate (Si_2IrO_4). 15–17, 21, 22, 29, 30, 32, 33, 35–37, 42, 44

SOC Spin-Orbit Coupling. 9, 11, 12, 14, 27

STO Strontium Titanate ($SiTiO_3$). 15, 37, 39

TMOs Transition Metal Oxides. 9–13

XMaS X-Ray Magnetic Scattering. 5, 20, 21

XRMS X-Ray Resonant Magnetic Scattering. 7, 24–28, 32–35, 37, 39, 41, 42

Contents

Chapter 1

Introduction

The intriguing properties pertaining to $3d$ transition metal oxides (TMOs) have attracted a substantial amount of attention in recent years. These properties, such as high temperature superconductivity in cuprates [1], colossal magnetoresistance in perovskite manganites [2] and multiferroicity [3] are the results of close competition between charge, spin, orbital and lattice degrees of freedom [4]. Some of this interest has recently migrated towards $5d$ oxides. The spatially extended $5d$ wavefunctions of these materials yield relatively weak electronic correlations ($\sim$ 0.5–3 eV) but strong crystal field effects ($\sim$ 1–5 eV) and, additionally, the large atomic number associated with $5d$ elements results in strong spin-orbit coupling ($\sim$ 0.1–1 eV) [5]. The similar energy scale of these three different types of interactions engenders a huge variety of behaviour in $5d$ TMOs, producing exciting physical properties and possibly new correlated ground states.

The primary task of this thesis is to determine the magnetic structure of epitaxial Sr_2IrO_4 thin films and compare it to bulk samples, as well as to investigate how this material behaves under the influence of magnetic fields and temperature. Thin film compounds may, due to strain exerted by a substrate, realize alternative crystal or magnetic structures and display fascinating new features. This chapter will proceed to introduce some fundamental concepts such as electronic correlation, spin-orbit coupling (SOC) and crystal field splitting in order to lay the theoretical foundation of the rest of this thesis.

1.1 Strongly correlated electron systems

Strongly correlated electron systems and their exotic properties cannot be understood within the conventional band structure theory where the electrons are treated as completely independent particles, i.e. non-correlated. In the general case, particles are not necessarily independent and the covariance of two correlated entities A and B

$$C_{AB} = \langle AB \rangle - \langle A \rangle \langle B \rangle \tag{1.1}$$

becomes finite [6]. Meaning that

$$\langle AB \rangle \neq \langle A \rangle \langle B \rangle. \tag{1.2}$$

Only if the covariance is zero the two different entities can be regarded as uncorrelated. In fact, electrons in TMOs are often strongly correlated, especially in the confined space of localized $3d$ bands.

A model that was proposed by J. Hubbard has successfully been used to describe $3d$ electrons in solids [7]. The model is built on the tight-binding approximation in which electrons are considered to occupy orbitals of their constituent atoms. It allows electrons to tunnel between different lattice sites as described by the "hopping" term $\mathcal{H}_H$ which contains $\mathbf{c}^\dagger_{i\sigma}$ ($\mathbf{c}_{i\sigma}$) operators that create (annihilate) an electron of spin $\sigma =\uparrow,\downarrow$ at lattice site i. The formation of electron bands in solids that promote this conduction is ultimately a consequence of non-filled overlapping orbitals.

The Hubbard model introduces an interaction term $\mathcal{H}_I$ to the Hamiltonian, which represents the Coulomb interaction between electrons in the same orbital. Thus, the Hubbard model describes the interplay between $\mathcal{H}_H$, which tries to delocalize the electrons, and $\mathcal{H}_I$ which tries to confine them [4]. The hopping integral is often denoted by the letter t since it represents the kinetic energy of the hopping electrons while the repulsion is denoted with a U since it represents the potential energy. The total Hamiltonian of the Hubbard model is then [4]

$$\mathcal{H} = \mathcal{H}_H + \mathcal{H}_I = \sum_{i,j}\sum_{\sigma} t_{ij}\mathbf{c}^\dagger_{i\sigma}\mathbf{c}_{j\sigma} + h.c. + U\sum_i \mathbf{n}_{i\uparrow}\mathbf{n}_{i\downarrow} \tag{1.3}$$

where $\mathbf{n}_{i\sigma} = \mathbf{c}^\dagger_{i\sigma}\mathbf{c}_{i\sigma}$ is the interaction term that by the anticommutation relations for fermions adds a potential energy U if a site is doubly occupied and $h.c.$ is the hermitian conjugate of the preceding term to ensure real eigenvalues and allow for reverse hopping $\mathbf{c}^\dagger_{j\sigma}\mathbf{c}_{i\sigma}$. Note that $t_{ij} = t_{ji}$ since the energy associated with hopping is the same in both directions.

Now consider a 1-dimensional hydrogen chain with one electron per atom and U and t chosen such that $U/t \to 0$ the system will be metallic because there is no energy penalty associated with double occupancy. The electrons are thus free to move from atom to atom, just as in band structure theory. If we instead let $U/t \to \infty$ double occupancy will be strongly suppressed and the system will become insulating. The electrons are in this case strongly correlated and from Eq. 1.2 one obtains $\langle \mathbf{n}_{i\uparrow}\mathbf{n}_{i\downarrow}\rangle \neq \langle \mathbf{n}_{i\uparrow}\rangle\langle \mathbf{n}_{i\downarrow}\rangle$. A metal-to-insulator transition will occur as a function of U/t and when U is large enough the system will become a so called Mott insulator, which is an insulating state that is common for $3d$ systems.

This model favours antiferromagnetic coupling between nearest neighbours since it is the only way electrons are allowed to hop between sites. If the spins were coupled ferromagnetically, hopping would not respect the Pauli exclusion principle [8].

1.2 From $3d$ to $5d$ complex oxides

1.2.1 Spin-orbit coupling

As discussed above, the $3d$ TMOs are characterized by the strong electron correlation of these systems. In contrast, the extended nature of $5d$ wavefunctions prohibits a strong electron correlation of $5d$ TMOs and leads to metallic conduction and non-magnetic states. However, these systems can instead be pushed into the correlated electron regime by an exceptionally strong spin-orbit interaction.

The angular magnetic moment produced by the orbiting electrons interacts with the intrinsic magnetic moment, the spin, of the electrons. The spin can either align parallel or antiparallel with the orbital magnetic field. This leads to the splitting (fine structure)

of degenerate energy levels since the preferred parallel state assumes a lower energy than the antiparallel state. A semiclassical derivation of the spin-orbit Hamiltonian yields [4]

$$\mathcal{H}_{SO} = \frac{Z^4 e^2 \hbar^2}{4\pi m_e^2 c^2 \epsilon_0 a_0^3 n^3 l(l+1)(2l+1)} \mathbf{L} \cdot \mathbf{S} = \lambda \mathbf{L} \cdot \mathbf{S} \tag{1.4}$$

where Z is the atomic number, e is the electron charge, $\hbar$ is the reduced Planck's constant, m_e is the electron mass, c is the speed of light in vacuum, ϵ_0 is the vacuum permittivity, a_o is the Bohr radius, n is the electron shell and l is the subshell.

The SOC constant λ has been found, theoretically and experimentally, to be on the order of $\sim 20 - 40$ meV for $3d$ ions [9] and $\sim 200 - 500$ meV for $5d$ ions [10]. It is evident that this discrepancy is a result of the significant contribution from the atomic number term Z^4/n^3 in λ ($3d$ ions have an atomic number of ~ 25 while $5d$ ions have an atomic number of ~ 75). If $\mathbf{L}$ and $\mathbf{S}$ are parallel the dot product in Eq. 1.4 will be positive while it will be negative if they are anitparallel, resulting in the spin-orbit splitting of the energy levels.

In order to more accurately describe $5d$ TMOs the strong spin-orbit Hamiltionian (Eq. 1.4) has to be included in the Hubbard model (Eq. 1.3) and the total Hamiltonian becomes

$$\mathcal{H} = \sum_{i,j} \sum_{\sigma} t_{ij} \mathbf{c}_{i\sigma}^{\dagger} \mathbf{c}_{j\sigma} + h.c. + U \sum_i \mathbf{n}_{i\uparrow} \mathbf{n}_{i\downarrow} + \lambda \sum_i \mathbf{L}_i \cdot \mathbf{S}_i, \tag{1.5}$$

while the SOC term is essentially neglected for $3d$ TMOs.

1.2.2 Crystal field splitting

The $5d$ orbitals are more spatially extended than $3d$ orbitals, the probability density of finding a d-electron in a $3d$ ion is largest around $r \sim 0.4$ Å, whereas for a $5d$ ion it is likely to be found around $r \sim 1$ Å [4]. The difference in shape and radial size of the electron clouds can affect the strength of the interaction with surrounding ligands in a crystal, causing the splitting of degenerate energy levels.

TMOs often take the form of 6-fold coordinated octahedrons where the d-metal ion is located in the middle with negatively charged ligands surrounding it (see top left of Figure 1.1 and 1.4). The spherical symmetry of a free single ion is broken by the octahedral cage and replaced by a cubic symmetry. The negatively charged ligands will exert a repulsive force on the electrons in the orbitals. The orbitals pointing directly towards the ligands, designated as e_g, will experience a larger repulsive force than the ones pointing in a 45° angle to them, designated as t_{2g} (see Figure 1.1). The electrons occupying the e_g manifold will thus be more easily ionized and the e_g state is shifted upwards in energy as compared to the t_{2g} state. This causes the otherwise degenerate states to split into an upper doublet e_g and a lower triplet t_{2g}.

The spatially confined $3d$ wavefunctions render the crystal field effects completely negligible for $3d$ ions. It is clear from Figure 1.2 that the Coulomb repulsion exerted by the ligands onto the different $3d$ orbitals should not vary significantly since $r_1^{3d} \approx r_2^{3d}$. For $5d$ orbitals, where $r_1^{5d} < r_2^{5d}$, the difference becomes appreciable, and thus a large crystal field splitting is also a consequence of the spatially extended $5d$ wavefunctions.

The energy splitting between the e_g and the t_{2g} states in Co and Ir has been estimated using a purely ionic model (neglecting covalency in the bonds) to be ~ 151 meV and ~ 2.34 eV respectively [4]. Even though the model is purely ionic, it offers an adequate

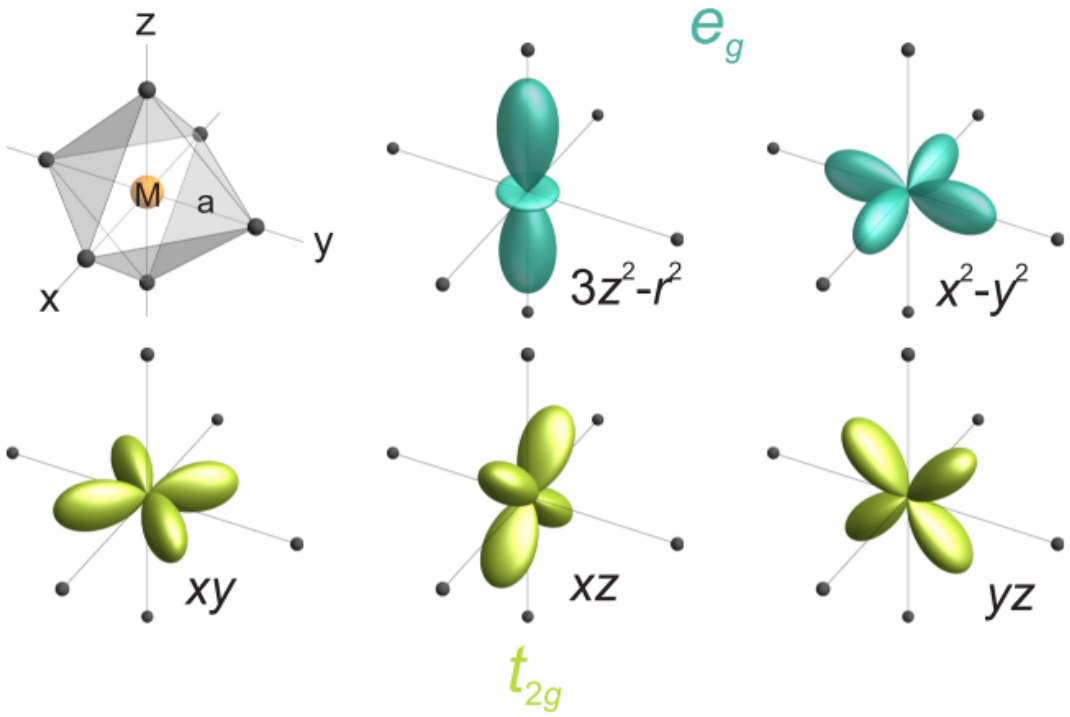

Figure 1.1: Top left of figure depicts the octahedral cage of negatively charged ligand ions surrounding the positively charged ion M. The other diagrams illustrate the five different orbital shapes of the d orbitals. Figure obtained from [4].

estimate of the change when moving from $3d$ to $5d$ systems as experimental values of crystal field splittings in $5d$ systems have been found to be ~ 3 eV [11]. This large energy gap ensures that it is more energetically favourable to minimize the strong crystal field energy than to follow Hund's rule. Consequently, as will be seen later in the case of $5d^5$ Sr_2IrO_4, the e_g state will be left completely vacant with all 5 electrons occupying the t_{2g} state. Forcing these $5d$ systems into assuming low spin configurations.

In essence, the small extension of the $3d$ orbitals is what confines the electrons in $3d$ TMOs and forces them to be strongly correlated. The $5d$ systems are not strongly correlated due to their large spatial extension, but instead experience a large crystal field splitting and a strong SOC that push them into a correlated regime. Thus, $5d$ systems have a spin-orbit induced Mott insulating state while $3d$ systems are driven into a Mott insulating state due to strong electron correlation.

Another important effect of the octahedral cage is that it prevents direct exchange between nearest ions due to the intermediate ligand oxygen. Direct hopping between d-orbitals is therefore unlikely in this situation and the antiferromagnetic coupling that is present in many TMOs is instead explained by the superexchange mechanism. The exchange interaction is here mediated between the ion d-orbitals through the oxygen p-orbitals. A 180° bonding angle of the metal-oxide-metal group favours antiferromagnetic bonding while a 90° bonding favours ferromagnetic coupling. In the 90° case the metal d-orbitals couple to orthogonal oxygen p-orbitals, prohibiting hopping from ion to ion since there is no hopping between p-orbitals of the same site. This leads to ferromagnetic coupling. In the case of 180° coupling, both d-orbitals couple to the same intermediate p-orbital, and thus an antiferromagnetic coupling is favoured since it allows hopping, see Figure 1.3 [8].

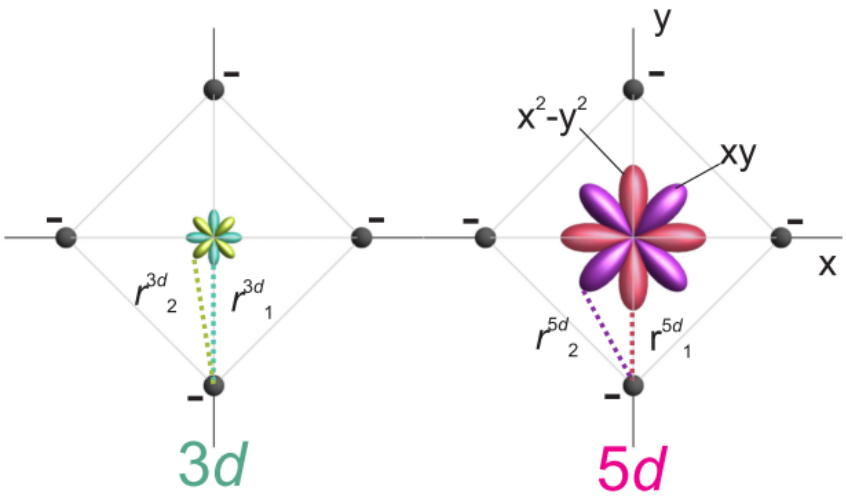

Figure 1.2: The radial extension of $3d$ and $5d$ orbitals. The relative distance from the negatively charged ligands to the different orbitals of the positive centre ion is a lot larger in the $5d$ case. Figure obtained from [4].

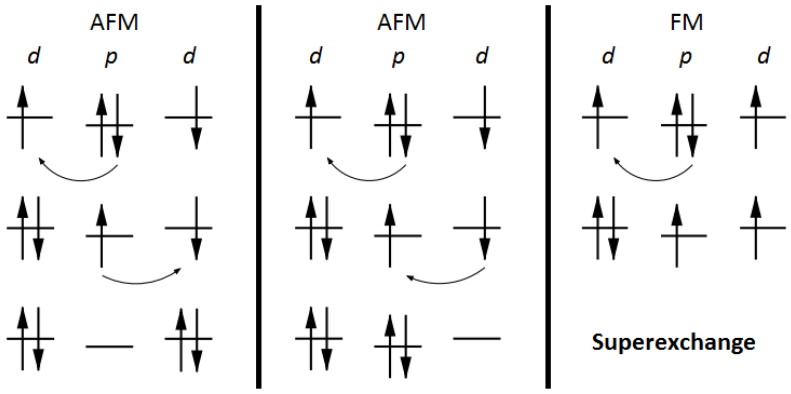

Figure 1.3: Schematic figure of the superexchange interaction. The metal d-orbitals interact through the centre (typically oxygen) p-orbitals.(Left and middle) Antiferromagnetic (AFM) coupling of the d-states allow hopping. (Right) Ferromagnetic (FM) coupling only allows one hopping process to occur, the second hop is suppressed by the Pauli exclusion principle. Figure adapted from [8].

1.3 The $j_{\text{eff}} = 1/2$ state

One of the exotic features of the $5d$ iridate compounds is the $j_{\text{eff}} = 1/2$ ground state. The strong correlation energy U and narrow energy band width leads to $S = 1/2$ Mott insulating ground states in the $3d$ TMOs. However, the strong spin-orbit interaction and crystal field splitting discussed independently above combine in $5d$ TMOs to generate a novel $j_{\text{eff}} = 1/2$ ground state.

Atomic iridium has a $[\text{Xe}]4f^{14}5d^{7}6s^{2}$ electron configuration, but when it is included in the octahedrons of a layered perovskite (see Chapter 2) it assumes an oxidation state of Ir^{+4} which reduces the electron configuration to $[\text{Xe}]4f^{14}5d^{5}$ where the $5d$ electrons are the valence electrons. First, consider these electrons stacking up according to Hund's rule, filling up all the l orbitals with one electron each (left of Figure 1.4). However, as explained in Section 1.2.2, the negative oxygen ligands that attracted some of the electrons exert a Coulomb repulsion on the $5d^5$ electrons, causing a crystal field splitting into the lower

t_{2g} triplet and the higher e_g doublet. The large energy splitting (~ 3 eV) between these two states ensures that all the electrons will end up in the t_{2g} manifold. The degeneracy of the t_{2g} states is once again broken due to SOC, producing a lower doublet $j_{\text{eff}} = 3/2$, with a 4-fold total angular momentum degeneracy and an upper singlet $j_{\text{eff}} = 1/2$ with a 2-fold total angular momentum degeneracy. These states arise from the fact that the effective total angular momentum of the t_{2g} manifold is $L = -1$ [12]. The ground state will thus be an electron hole in this $j_{\text{eff}} = 1/2$ state; this turns out to be important as will be shown later in Section 3.2.

An alternative way of explaining this that might be more "intuitive" is by first considering SOC on the $5d$ levels into a $j = 5/2$ triplet and a $j = 3/2$ doublet. The cubic crystal field then forces two of the $j = 5/2$ orbitals upwards in energy (the two e_g states), effectively branching off the $j_{\text{eff}} = 1/2$ state [13]. The $j_{\text{eff}} = 1/2$ state is thus energetically higher than the $j_{\text{eff}} = 3/2$ state, not conforming with Hund's rule. This is because it originally comes from the $j_{5/2}$ state. It should be mentioned that the c-axis (z-axis in Figure 1.4) of the IrO_6 octahedron is elongated by 4% in bulk Sr_2IrO_4 [14]. The cubic symmetry is therefore not perfect, but this small deviation from the assumed $I4_1/acd$ space group should most likely not affect the magnetic structure in a significant way.

Coulomb interaction and SOC force the system into an insulating state by the splitting (~ 0.5 eV) of the $j_{\text{eff}} = 1/2$ state into lower and upper Hubbard bands [15]. This band gap is what makes the system magnetic, if it would vanish the material would be conducting and all magnetism would be lost.

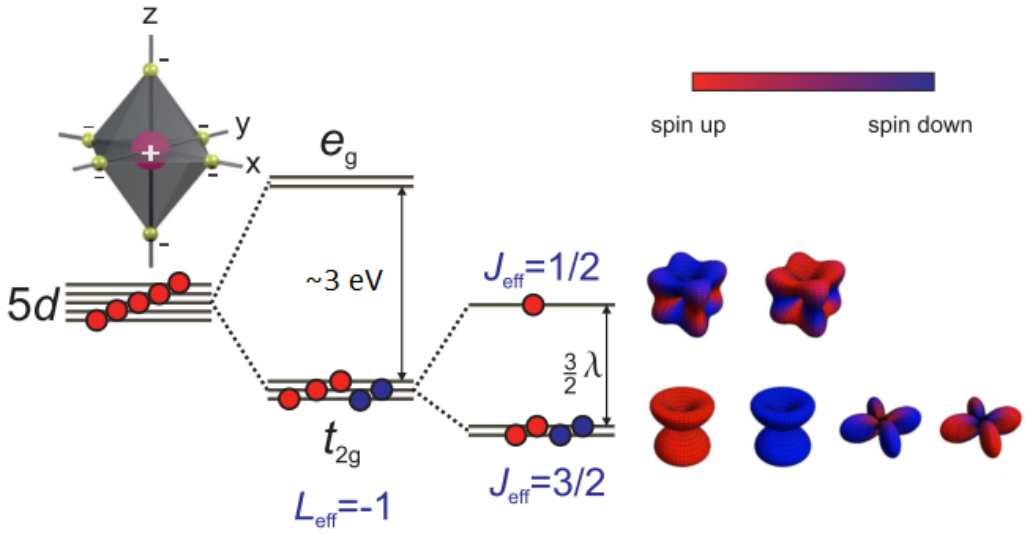

Figure 1.4: The formation of the novel $j_{\text{eff}} = 1/2$ state due to SOC and crystal field effects. For $5d$ systems the crystal field splitting is usually ~ 3 eV while the SOC constant $\lambda \approx 200 - 500$ meV. Notice the interesting topology of the $j_{\text{eff}} = 1/2$. Figure obtained from [4].

Chapter 2

Samples and Probes

The samples investigated were thin epitaxial films of the layered perovskite[1] Sr_2IrO_4 (SIO) (space group $I4_1/acd$ with lattice parameters $a = b = 5.48$ Å, $c = 25.8$ Å [14]) on a (001)-oriented cubic preovskite $SrTiO_3$ (STO) substrate (space group $Pm\bar{3}m$ with lattice parameter 3.905 Å at room temperature [17]). The STO lattice parameter of 3.905 Å results in an STO (110) lattice distance of 5.52 Å ($3.905 \cdot \sqrt{2} = 5.52$) which is similar to the 5.48 Å of SIO and thus the SIO film is rotated 45° with respect to the substrate.

Previous neutron [18] and x-ray resonant scattering [19] experiments performed on bulk SIO have deduced the Ir–O bond length and bond angles, resulting in a structure described by the canting of the octahedra shown in Figure 2.1. The neutron study reported a canting of $\phi = 13(1)^\circ$ while the X-ray resonant scattering study reported a spin canting angle $\phi = 12.2(8)$ and a rotation of the octahedral cages of $\sim 11.8^\circ$. The octahedral cages and the spin moments are thus seemingly related.

In this thesis, three different samples of different thickness were studied, 120 nm, 80 nm and 30 nm. No magnetic peaks were found on the 30 nm sample, perhaps due to a non-relaxed (distorted) structure from an overwhelming strain exerted by the STO substrate. In thicker samples this strain might only effect the parts of the sample closest to the substrate while gradually relaxing further away from it, leaving a substantial piece of relaxed, ordered structure to measure on. Another explanation could simply be that the sample was too thin and not enough scattering points were present to result in a detectable signal. This result for the 30 nm film is still to be clarified and the issue might be resolved at a higher flux beam line in the future. The 80 nm sample did produce magnetic peaks but this sample was not extensively studied. The main focus of this thesis will be on the 120 nm sample on which all following measurement were made. It is important to mention that the STO has a phase transition at a temperature of ~ 110 K, this will be important later on in Chapter 4.

2.1 Epitaxial films by pulsed laser deposition

A number of various epitaxial growth methods of oxide thin films (such as sputtering, spin coating and molecular beam epitaxy (MBE)) have been developed to circumvent the

[1] Perovskite is the crystal structure of any material with the chemical formula XYZ_3 where X and Y are cations and Z is an anion bonding the two, such as $CaTiO_3$ [16]. A layered perovskite consists of cubic perovskite layers separated by intermediate layers of other crystal structures. The intermediate layers can take many different forms but in this case it is a single layer of Sr atoms (see Figure 2.1) resulting in the chemical formula Sr_2IrO_4.

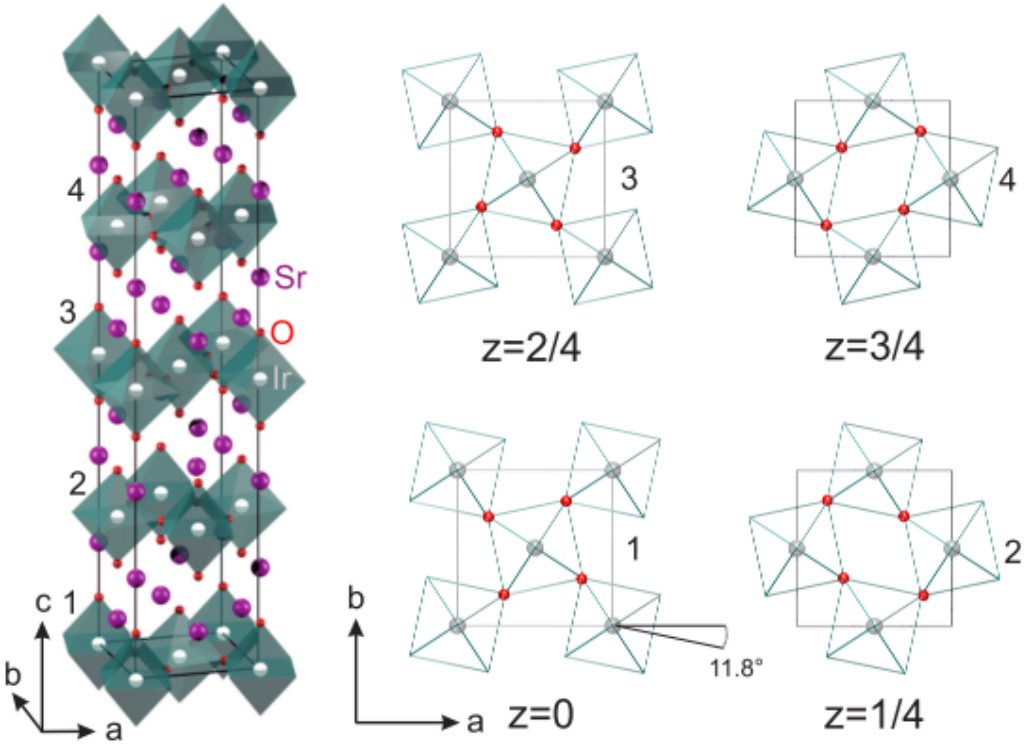

Figure 2.1: Structure of bulk SIO (space group $I4_1/acd$), lattice parameters: $a = b = 5.48$ Å and $c = 25.8$ Å. Z is the interplanar distance along c in units of one unit cell. Figure obtained from [4].

challenges of growth by thermal evaporation, where the starting materials have melting points well above 1,000 °C [20]. The iridate films studied in this thesis were grown by S. Geprägs of the Walther Meißner-Institut, using a successful technique called pulsed laser deposition (PLD), sometimes referred to as laser-MBE.

The experimental set-up of a PLD process chamber can be seen in Figure 2.2(a). In PLD, a pulsed ultraviolet laser is focused onto the target material. The photons cause electronic excitations where the energy then rapidly dissipates into core motion and bond breaking, finally resulting in the emission of ions and atoms in the so called "plasma plume" (inset in Figure 2.2(a)) [22]. This type of removal of material from a solid is called laser ablation. The PLD technique stoichiometrically transfers material from the target to the sample substrate via the plasma plume [23]. Several of these, usually polycrystalline targets, can be placed on a rotatable plate, or "target carousel", for a quick and easy exchange of target materials.

The quality of PLD grown films was greatly improved by the introduction of RHEED (reflection high-energy electron diffraction) since it provides *in situ* characterization of the films. RHEED consists of an electron gun that fires high energy electrons ($\sim$ 10 keV) onto the sample surface and a fluorescent screen that images the resulting interference pattern [23]. The technique is highly surface sensitive because the electron beam strikes the sample at a high grazing angle [24]. By studying the intensity of the diffracted beam one can determine how many monolayers that have been deposited onto the film. When new particles adsorb on a flat monolayer the order will decrease, causing the diffracted intensity to decrease. As half of the surface has been covered by adsorbates the order, and thus the diffracted intensity, has reached its minimum. The intensity then increases as more particles are adsorbed and it finally reaches a maximum when a complete monolayer

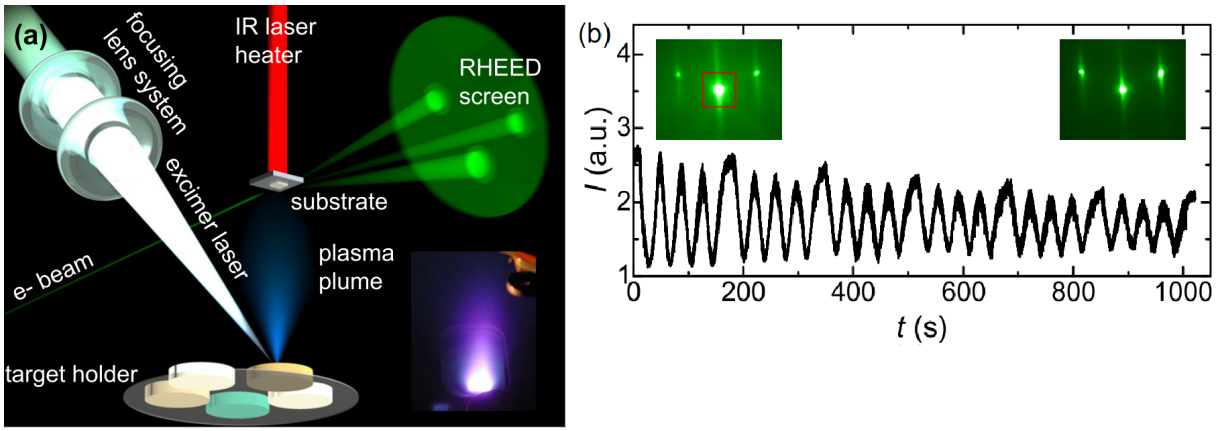

Figure 2.2: (a) Schematic figure of the PLD process chamber. The inset is a photograph of the plasma plume. (b) RHEED intensity oscillations recorded during growth of 50 nm thick SIO. The insets illustrate the RHEED pattern at the beginning (left) and at the end (right) of the growth process. Notice how the peak maxima decrease in intensity as more layers are deposited. This is due to the surface moving away from the beam focus when the film grows. Figure obtained from [21].

has been deposited, at which the order is at its maximum again. This behaviour produces so called intensity oscillations that can be seen in Figure 2.2(b). Every intensity maxima corresponds to a complete, single monolayer. The average intensity of these oscillations decreases due to the fact that the surface of the film moves away from the focus point of the electron beam as the film grows.

2.2 Production of synchrotron x-rays

X-ray diffraction is a powerful tool commonly used to deduce the crystal structure of solids. An attempt to explain how this is done is found in the next chapter, however, first a description of how x-rays are produced will be provided. The experiments in this thesis require a well collimated, coherent, tunable, yet powerful x-ray source, which is why we turned to synchrotron radiation.

An accelerated charged particle emits electromagnetic radiation. This can be understood quite intuitively by considering the oscillation of the field lines produced by an oscillating (accelerated) charged particle. This phenomenon is utilized in a regular dipole antenna where electrons are accelerated back and forth in a wire using an alternating current. The field lines parallel to the direction of motion are not "disturbed", and thus no radiation is emitted in this direction. The maximum flux of an antenna is instead directed perpendicular to the motion of the electrons, where maximum oscillation of the field lines occur.

A synchrotron radiation source also takes advantage of this phenomenon as the electrons are travelling around the storage ring. When the electrons are bent they are accelerated towards the centre of the ring. For slow electrons, the angular distribution of the emitted power follows a $\sin^2(\theta)$ behaviour where $\theta = 0$ is parallel to the direction of acceleration, as seen in Figure 2.3(a). When the electrons approach the speed of light, the emitted radiation becomes collimated in the forward direction with an opening angle of $1/\gamma$ (where $\gamma = \frac{1}{\sqrt{1-\beta^2}}$, and β is the ratio of the particle velocity to the speed of light),

as seen in Figure 2.3(b) [25]. This effect is known as relativistic aberration and it was derived by Einstein in 1905 [26].

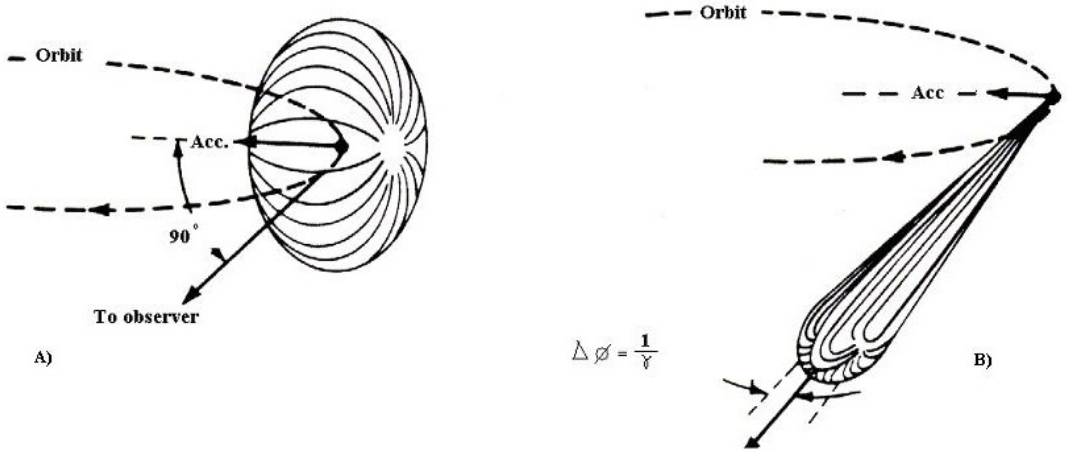

Figure 2.3: a) A slow electron that is accelerated towards the centre of the ring will emit radiation similarly to that of an oscillating dipole. b) When the electrons become ultrarelativistic the radiation becomes collimated in the forward direction with an opening angle of $1/\gamma$. Figure by R. Bartolini, John Adams Institute, 2013.

Provided that the electrons are energetic enough, the output will be a well collimated beam with a high photon flux. An important feature of the bending magnet spectrum is that it produces a continuous spectrum (see Figure 2.4). The attentive reader may notice that the bending magnet spectrum resembles the spectrum of *bremsstrahlung* produced by a standard tube source. This is evidently a consequence of the similarities in the production of radiation between the two cases. Radiation is emitted when electrons are deflected and decelerated by an atomic nucleus in a tube source, and by a macroscopic magnetic field in a synchrotron. One important difference however, is that the drop off photon energy is never the full kinetic energy of the electrons since they are never brought to a full stop in a synchrotron storage ring, as opposed to in the target material of a tube source.

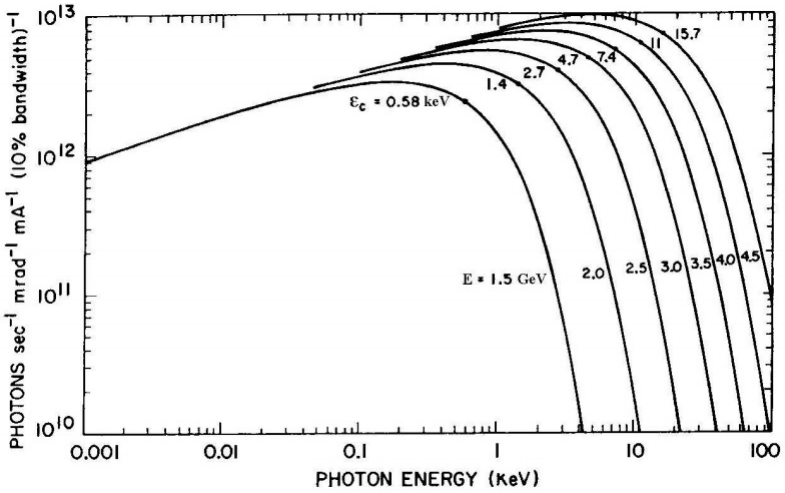

Figure 2.4: Spectrum of a dipole bending magnet at a few different electron energies. Figure obtained from [25].

It has now been shown how a continuous spectrum of x-rays with high flux and collimation is achieved. However, one can do even better by introducing magnetic arrays in the straight sections of the synchrotron, called insertion devices. These magnetic arrays consist of a large number of permanent magnets that create an alternating static magnetic field perpendicular to the direction of electron motion. This forces the beam to undulate (or wiggle) and thus emit radiation, hence the names of these insertion devices are undulators and wigglers.

Although undulators and a wigglers simply cause transverse oscillations in the beam, there is a fundamental difference between the two. The magnetic array of a wiggler simply wiggles the beam back and forth as if it was a number of consecutive bending magnets. In an undulator however, the magnetic field strength and periodicity is tuned to cause interference between the radiation emitted at different magnetic poles. This yields enhanced emission at a fundamental frequency and its harmonics [27]. An example of what an undulator spectrum can look like is seen in Figure 2.5

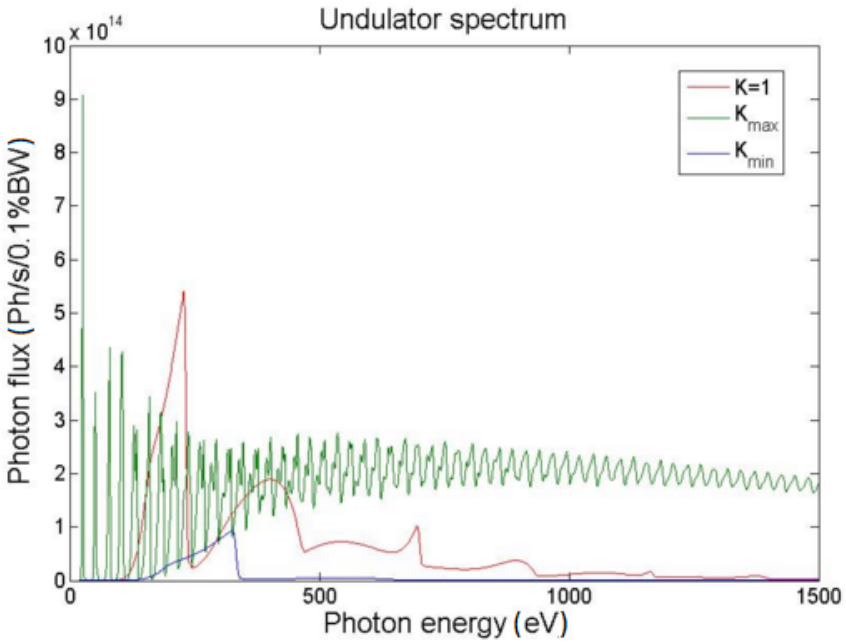

Figure 2.5: An example of what an undulator spectrum can look like at three different magnetic field strengths. One can clearly see the different harmonics. The spectrum is a simulation of the SPECIES beamline at MAX II using SPECTRA, version 10.0.2 (software from SPring-8).

The Angstrom sized wavelength of x-rays is produced in undulators by the macroscopic, centimetre sized periodicity in the magnetic array. The magnetic period L of the undulator, as seen by the electrons, is Lorentz contracted to L/γ, which is also the wavelength of the emitted light in the electron rest frame. When transforming to the laboratory frame, the Doppler shift of the emitted light introduces another factor of γ resulting in the final wavelength of the emitted light to be $\approx L/2\gamma^2$ [28]. If γ is sufficiently large, the produced light will be in the x-ray regime.

2.3 The XMaS beamline experimental set-up

The experiments were performed using the XMaS (X-ray Magnetic Scattering) bending magnet beamline (BM28) at the European Synchrotron Radiation Facility (ESRF) in Grenoble, France.

2.3.1 Optical elements

The XMaS beamline is schematically illustrated in Figure 2.6 with all optical elements marked out. Here, only a short description of the most relevant optical elements will be provided.

The desired photon energy is selected in the double-crystal monochromator that consists of two Si (111) crystals [29]. The monochromator selects the desired photon energy according to Bragg's law (see next chapter) by coupled rotation of the two silicon crystals. The monochromator is continuously tunable in the energy range of 2.4 to 15 keV which comprises the desired photon energy (11.215 keV) of our experiments. The sample was placed on the sample stage of a Huber diffractometer (see Figure 2.7) that allows for sample rotation in any desired orientation. A large degree of freedom is essential for single crystal diffraction experiments (see next chapter). The three different angels of sample rotation are defined in the figure as ψ, θ and χ.

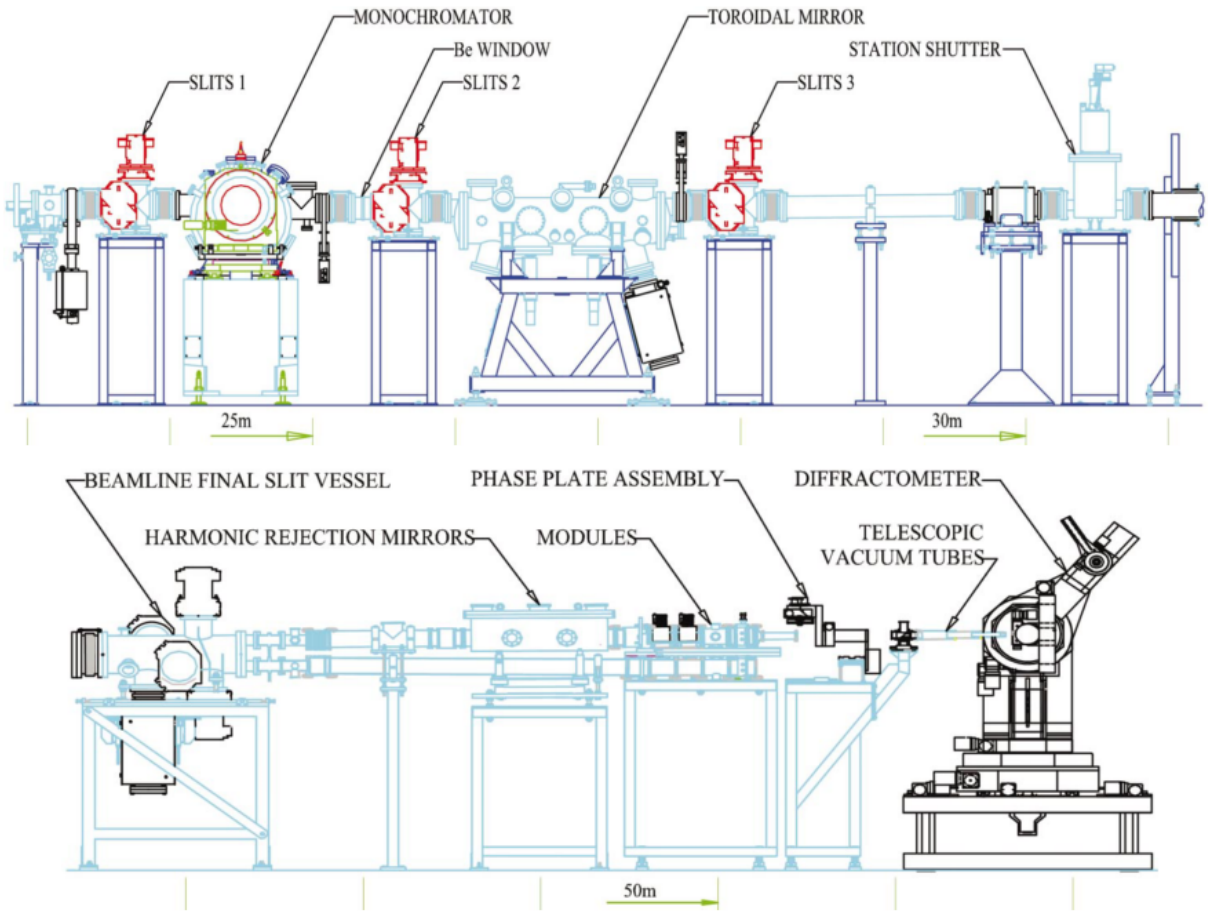

Figure 2.6: (Top) Schematic view of the beamline and (bottom) beam conditioning in the experimental hutch with optical elements marked out. Figure obtained from [29]

As will be seen in the next chapters, the ability to determine the polarization of the

scattered light is crucial in these experiments. The polarization of the scattered light was analysed with a Au (333) crystal that was placed after the SIO sample. The function of the polarization analyser is to distinguish between x-rays with a polarization parallel (π) with and perpendicular (σ) to the plane of incidence, as shown in Figure 3.3. Ideally, the polarization analyser is placed at a 45° angle with respect to the direction of the incident beam. This is in fact, for π polarized x-rays, the only angle where the electric field vector of the incident x-rays is parallel to the direction of the scattered beam. The electric field vector of the incident beam will thus induce electron oscillations parallel with the direction of a scattered beam for this geometry. As we learned from previous section, there is no light emitted from an oscillating dipole in the direction of oscillation. Therefore π polarized light cannot be scattered at a 45° angle, whereas σ polarized light can. By allowing coupled, 90° rotation of the gold crystal and the detector around the axis of the incident light, one can choose to discriminate either of the two orthogonal states of polarization. This way, one can determine if the beam scattered by the sample is σ or π polarized.

An Au (333) crystal was chosen since the Bragg angle corresponding to the desired photon energy (11.215 keV) is close to 45°. It is however not exactly 45°, which means that a small component of the π polarized light will be reflected. This means that we cannot completely discriminate one state from the other which results in cross contamination. Furthermore, the x-ray beam from the synchrotron is not perfectly polarized, this also leads to some cross contamination.

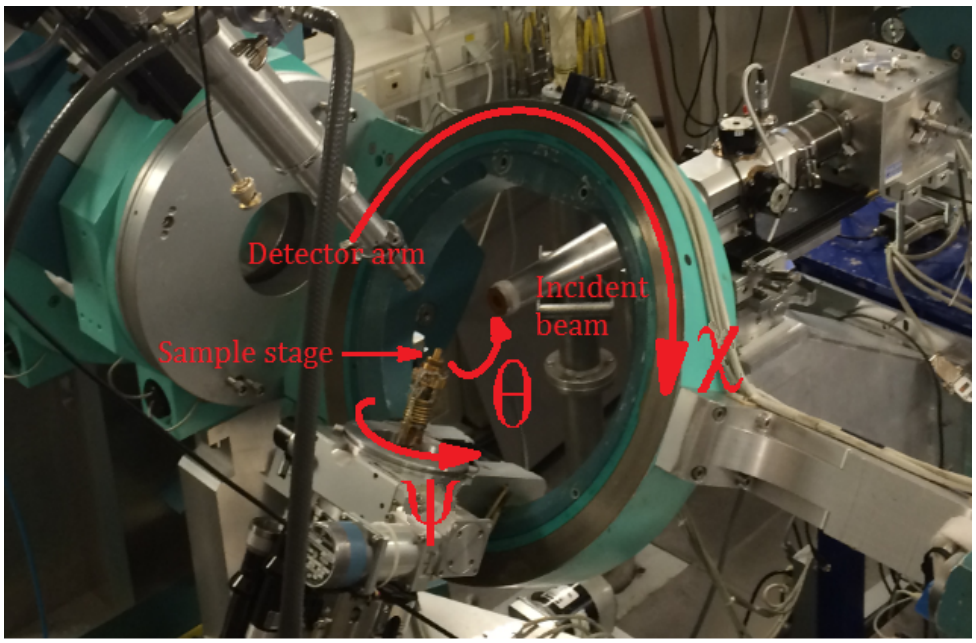

Figure 2.7: The Huber diffractometer at the XMaS beamline.

2.3.2 Sample environment

Since SIO only acquires its antiferromagnetic structure at temperatures below $\sim$ 220 K, a helium closed cycle cryostat was used to cool the sample and keep it stable at temperatures as low as 10 K. The cryostat works by means of rapid expansion of helium gas in a closed circuit which cools the gas according to the ideal gas law. The helium gas is forced into the cryostat through a high pressure gas reserve where it is then expanded through the release

of a piston. The rapid decrease in pressure cools the gas which is then allowed to flow back into a low pressure gas reserve where it is reccompressed. This process is then repeated. A closed cycle cryostat does not need refilling of helium, it does however consume a fair amount of electricity. The sample is covered with a beryllium capsule that keeps the sample under vacuum. If in contact with air, the cold sample would cause formation of ice droplets that would absorb the x-rays and interfere with the measurements. The beryllium capsule itself is a light element, virtually transparent to x-rays.

The intention of doing measurements on SIO in magnetic fields was realized in two different ways. The first set of in-field measurements were performed simply by the use of permanent magnets (see Figure 2.8(a)). The field over the sample was measured to be $\sim$ 200 mT along the *b*-axis of the SIO film. This set-up was used for all in-field measurements except the last measurement where a magnetic field dependence was performed. For this, an electromagnet was used (see Figure 2.8(b)) where the magnetic field was varied between -500 and 500 mT.

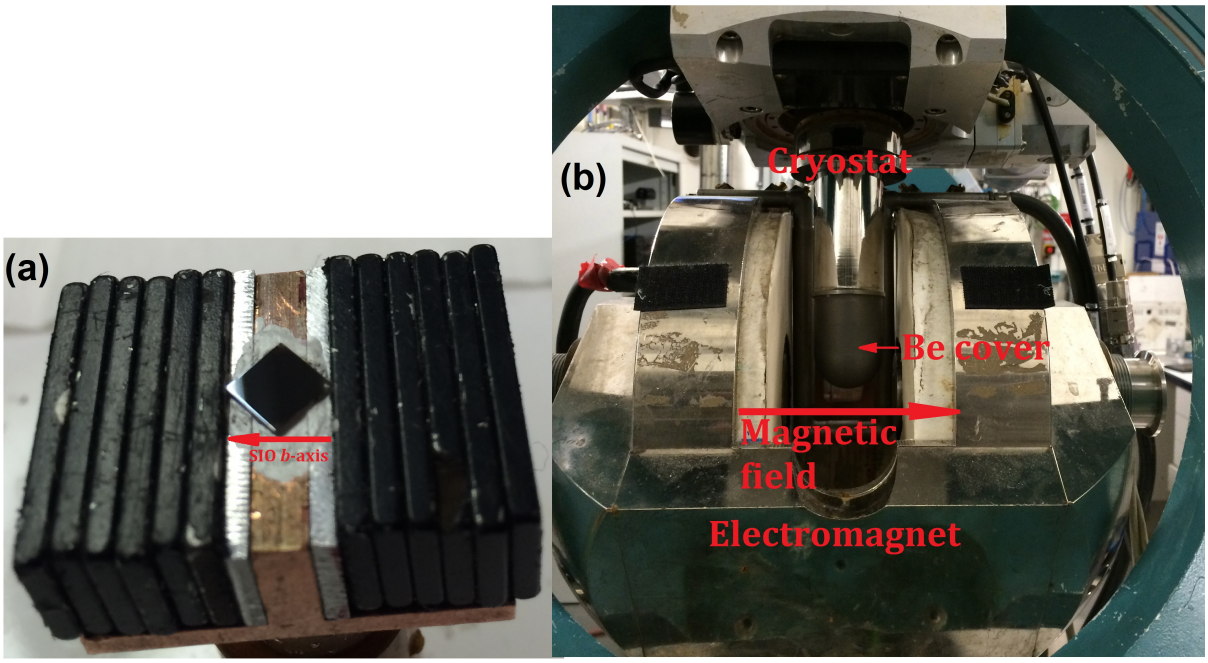

Figure 2.8: (a) The sample is placed between permanent magnets producing a field of $\sim$ 200 mT. (b) Electromagnet used for magnetic field scans from -500 to 500 mT.

Chapter 3

X-Ray Diffraction and X-Ray Resonant Magnetic Scattering

When electromagnetic waves impinge atoms the electrons begin to oscillate and re-radiate the waves (Thomson scattering) in all directions. When several atoms are close to each other as in a crystal lattice, the re-radiated waves from each atom interferes and creates a diffraction pattern. By carefully studying the diffraction pattern one can try to determine the structure of the lattice. When light and matter do not interact simply through Thomson scattering, but through atomic electron transitions, things becomes a bit more complicated. This chapter will shed some light on how x-ray diffraction can be used to determine the atomic, as well as the magnetic structure of a lattice.

3.1 X-ray diffraction

When visible light is incident on a flat surface such as a mirror it is reflected with the same angle (specular reflection). When the wavelength of the light is comparable or smaller to the interatomic distances within a solid one may find diffracted beams in other directions [30]. Bragg's law of diffraction was proposed by William Henry and William Lawrence Bragg (father and son) in 1913 [31]. It relies on a monochromatic, coherent beam of light with wavelength λ, incident with an angle θ onto a crystal with a lattice plane distance d (see Figure 3.1). The phase difference between two rays scattered off of two adjacent planes is $2d\sin(\theta)$. Constructive interference then occurs when this phase difference is equal to an integer number n of the wavelength. This gives the Bragg equation

$$2d\sin(\theta) = n\lambda \tag{3.1}$$

It is clear that this equation is only satisfied when $\lambda \leq 2d$. Using a known wavelength one can determine the lattice spacing d by measuring the scattering angle 2θ (the detector angle).

In the general case a crystal is not isotropic and the lattice spacing varies in different directions. In order to deduce the crystal structure one has to measure the lattice distance of several planes. These planes are uniquely defined by the Miller index notation that uses three numbers h, k and l to specify the (inverse of the) intersection of the plane (hkl) with the crystallographic axes a, b and c. Parallel planes such as (001) and (002) only differ by the distance at which they intersect the crystallographic axes. The lattice distance d associated with these two planes is therefore different, resulting in different scattering

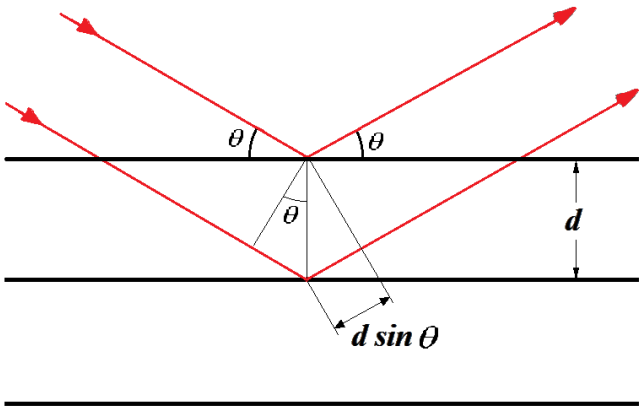

Figure 3.1: A monochromatic, coherent beam of light incident on atomic planes. The phase difference of $2d\sin(\theta)$ between two scattered rays can be appreciated geometrically in the figure.

angles. In reality, it is the atoms that scatter light and not the planes themselves, and the diffraction peak corresponding to the (002) plane is actually the second order maximum of the (001) plane. In this case n from Eq. 3.1 is the order of diffraction. It is however useful to regard these higher order peaks as diffraction from virtual planes.

Some diffraction peaks can be tricky to find in a diffraction experiment since they depend on the exact adjustment of three different angles θ, χ and ψ (rotation around the x, y and z axes respectively, see Figure 2.7). In practice one usually determines the crystal structure of a compound by looking at powder samples. The random crystalline orientation of the powdered crystals ideally ensures that all planes are equally represented. The rotational averaging results in diffraction rings instead of diffraction spots, tremendously simplifying the experiment as one only has to scan over one angle instead of three.

Since powdering our samples would defeat the purpose of studying thin films we are forced to use a goniometer and find the relevant reflections by adjusting θ, χ and ψ. To further complicate things, we are interested in the magnetic structure of our sample which means we cannot rely on Thomson scattering, but have to probe an atomic electron transition to the magnetic $j_{\text{eff}} = 1/2$ state.

3.2 XRMS - probing the $j_{\text{eff}} = 1/2$ state

Just as x-ray diffraction can be used to determine the atomic positions in an ordered crystal lattice, it can be used to determine the magnetic structure of ordered magnetic moments. To deduce the magnetic structure, x-ray resonant magnetic scattering (XRMS) can be used, which is a diffraction technique that relies on the ability of the incoming light to drive an atomic electron transition to a magnetic state. The wavelength of the light has to be tuned to a certain transition to ensure a reasonable interaction probability, which is why a tunable light source is essential for the experiments in this thesis. This stands in contrast to normal x-ray scattering which is independent of the wavelength (as long as $\lambda \leq 2d$ is satisfied) since the fundamental light-matter interaction is Thomson scattering.

The relevant transition of the experiments in this thesis is the $2p_{3/2}$ state to the $j_{\text{eff}} = 1/2$ state, also know as the L_3 edge (see Figure 3.2). This transition was chosen as it is an E1 (electric dipole) transition and should be quite strong since it follows the selection rule $\Delta L = \pm 1$. Furthermore, it was chosen over the L_2 edge not only because the statistical branching ratio $I_{L_3}/I_{L_2} = 2$ (since there are twice as many states in the $2p_{3/2}$ state than in the $2p_{1/2}$ state) but because the observed branching ratio in Sr_2IrO_4 is $I_{L_3}/I_{L_2} \approx 7$ [5]. Due to dipole selection rules, the branching ratio depends not only on the amount of final states in the manifolds but on the valence band spin-orbit coupling as well as the electrostatic interactions between core hole and valence band. The branching ratio can be proven to be proportional to the expectation value of the spin-orbit operator $\langle \mathbf{L} \cdot \mathbf{S} \rangle$, not to be confused with the spin-orbit Hamiltonian, H_{SO} [32–34]. The reason for this large branching ratio is thus due to a strong spin-orbit interaction.

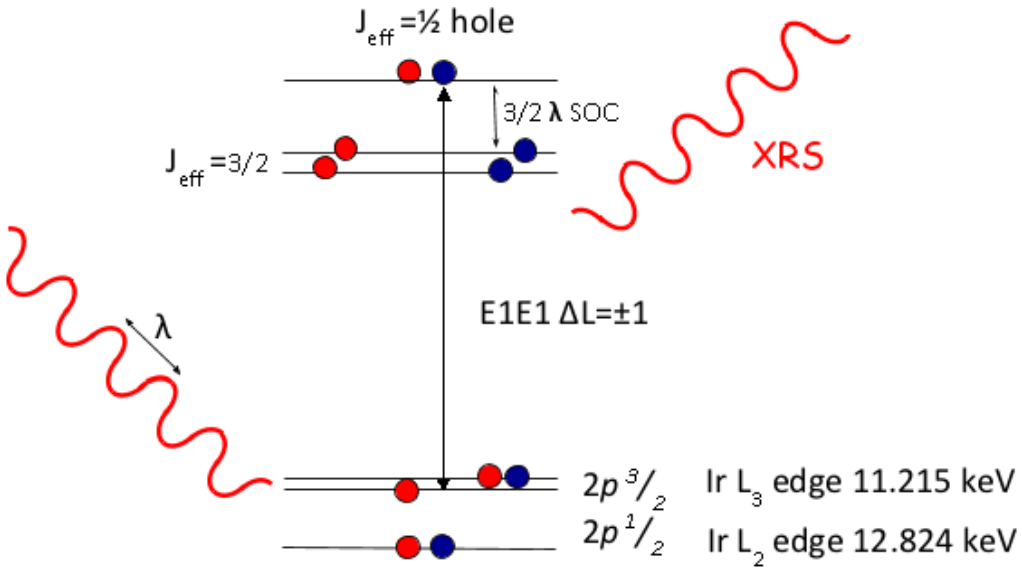

Figure 3.2: The transition probed by XRMS. Figure adapted from [4].

X-ray scattering can be thought of as light scattering by electron charges. In XRMS however, the light is scattered by the electron spins. Therefore, this process is dependent on the size of the magnetic moments as well as their orientation relative to the polarization of the impinging light. An important feature of XRMS is that the polarization state of the incident wave can be changed in the scattering process. An incoming wavevector $\mathbf{k}$ with σ polarization will thus result in a final wavevector $\mathbf{k}'$ with a π' polarization (see Figure 3.3). This stands in direct contrast with Thomson scattering where the induced electron oscillations are limited to the plane of polarization, the re-radiated waves of the electrons are therefore bound to retain the state of polarization of the incident light.

To further explain this, we turn to the scattering amplitude of XRMS which can be written as [35, 36]

$$\mathcal{A}_{\text{j,E1}}^{\text{REXS}} = (\boldsymbol{\epsilon} \cdot \boldsymbol{\epsilon}')F^0 - i(\boldsymbol{\epsilon} \times \boldsymbol{\epsilon}') \cdot \hat{\mathbf{z}}_j F^1 + (\boldsymbol{\epsilon}' \cdot \hat{\mathbf{z}}_j)F^2 \tag{3.2}$$

where $\boldsymbol{\epsilon}$ is the unit polarization vector, $\hat{\mathbf{z}}_j$ is a unit vector pointing in the directions of the

jth magnetic moment and with

$$F^0 = (3/4k)[F_{11} + F_{1\bar{1}}] \tag{3.3}$$
$$F^1 = (3/4k)[F_{11} - F_{1\bar{1}}] \tag{3.4}$$
$$F^2 = (3/4k)[2F_{10} - F_{11} - F_{1\bar{1}}]. \tag{3.5}$$

The F_{LM} factors are related to the strength of the resonance based on atomic properties. The F^n factors of Eq 3.2 will be ignored in the following. The coordinate system of the scattering geometry is illustrated in Figure 3.3 and the scattering amplitude of this scenario will be discussed on the basis of the two orthogonal polarization states σ and π. This leaves us with four possible scattering situations expressed in a 2×2 matrix

$$(\boldsymbol{\epsilon}, \boldsymbol{\epsilon}') = \begin{pmatrix} (\boldsymbol{\epsilon}_\sigma, \boldsymbol{\epsilon}'_\sigma) & (\boldsymbol{\epsilon}_\sigma, \boldsymbol{\epsilon}'_\pi) \\ (\boldsymbol{\epsilon}_\pi, \boldsymbol{\epsilon}'_\sigma) & (\boldsymbol{\epsilon}_\pi, \boldsymbol{\epsilon}'_\pi) \end{pmatrix}. \tag{3.6}$$

The first term in Eq. 3.2 for these four situations becomes

$$\boldsymbol{\epsilon} \cdot \boldsymbol{\epsilon}' = \begin{pmatrix} 1 & 0 \\ 0 & \widehat{\mathbf{k}} \cdot \widehat{\mathbf{k}}' \end{pmatrix}. \tag{3.7}$$

It is clear from this result that the first term of Eq. 3.2, which is independent of $\widehat{\mathbf{z}}_j$, described Thomson scattering where a change in polarization is impossible. Interestingly, this term also explains the polarization analyser, when the two wave vectors are orthogonal the scalar product in the $\pi\pi'$-channel becomes zero. The second term of Eq. 3.2 becomes

$$(\boldsymbol{\epsilon} \times \boldsymbol{\epsilon}') \cdot \widehat{\mathbf{z}}_j = \begin{pmatrix} 0 & -\widehat{\mathbf{k}}' \\ \widehat{\mathbf{k}} & \widehat{\mathbf{k}}' \times \widehat{\mathbf{k}} \end{pmatrix} \cdot \widehat{\mathbf{z}}_j \tag{3.8}$$

This term, which does depend on $\widehat{\mathbf{z}}_j$ represents XRMS. One can see that the case of $(\boldsymbol{\epsilon}_\sigma, \boldsymbol{\epsilon}'_\sigma)$ is forbidden, as opposed to in the first term. This fact will be used later on in the experiments to distinguish between XRMS and Thomson scattering. The third term of Eq. 3.2 will be omitted as it is not relevant for iridium oxides [4]. The XRMS amplitude can thus be written as

$$\begin{aligned} \mathcal{A}^{\mathrm{XRMS}}_{\mathrm{j,E1}} &= -iF^1 \begin{pmatrix} 0 & -\widehat{\mathbf{k}}' \cdot \widehat{\mathbf{z}}_j \\ \widehat{\mathbf{k}} \cdot \widehat{\mathbf{z}}_j & (\widehat{\mathbf{k}} \times \widehat{\mathbf{k}}') \cdot \widehat{\mathbf{z}}_j \end{pmatrix} \\ &= -iF^1 \begin{pmatrix} 0 & z_3 \sin\theta - z_1 \cos\theta \\ z_1 \cos\theta + z_3 \sin\theta & -z_2 \sin 2\theta \end{pmatrix} \end{aligned} \tag{3.9}$$

where z_i are the spin components along the $\widehat{\mathbf{u}}_i$-axes from Figure 3.3 and θ is the Bragg angle. Eq. 3.9 shows which spin components that contribute to the resonant magnetic scattering and we can see that the $\sigma\pi'$-channel does not depend on z_2. This will be used in Chapter 4 when we attempt to determine the directions of the spins in a so called azimuthal dependence. This scattering amplitude only applies to single ions, in order to account for scattering from multiple ions the contribution from each individual ion has to be summed; this is further discussed in the following section.

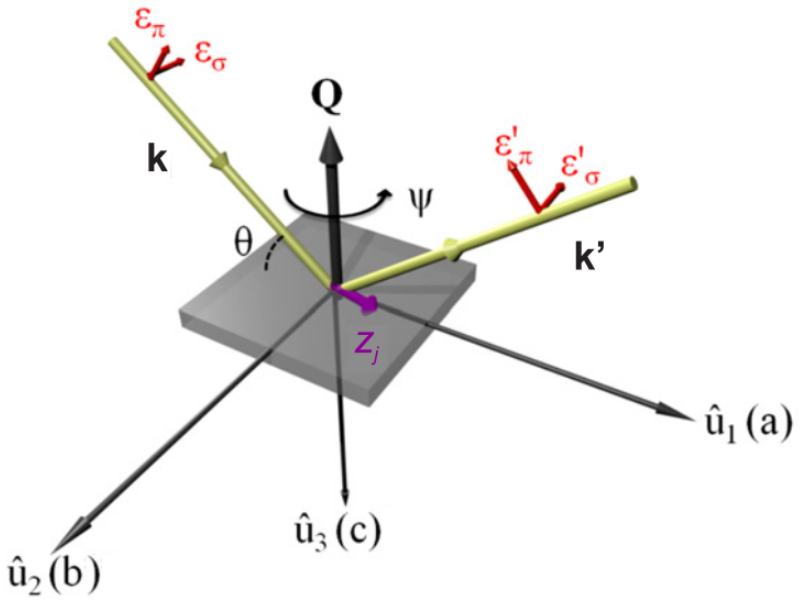

Figure 3.3: Scattering geometry and coordinate system of XRMS. Figure adapted from [19].

So far, the scattering amplitude has only been considered geometrically and one might wonder where the actual spins come into play. The scattering cross-section of these experiments consists of Thomson, resonant and non-resonant scattering terms. Thomson scattering is independent of the spins and only contains a dependence on the Fourier transform of the electron density, as will be seen in the next section. Non-resonant scattering has a direct dependence on the spins, but is weak and has not been used in this thesis work. The resonant scattering amplitude can be written as [4]

$$\mathcal{A}_{res} \approx -\frac{1}{m}\sum_{c}\sum_{ij}\frac{E_a - E_c}{\hbar\omega_{\mathbf{k}}} \left(\frac{\langle b|(\boldsymbol{\epsilon}'\cdot\mathbf{p}_i - i\hbar(\mathbf{k}'\times\boldsymbol{\epsilon}')\cdot\mathbf{s}_i)e^{-i\mathbf{k}'\cdot\mathbf{r}_i}|c\rangle\langle c|(\boldsymbol{\epsilon}\cdot\mathbf{p}_j + i\hbar(\mathbf{k}\times\boldsymbol{\epsilon})\cdot\mathbf{s}_j)e^{i\mathbf{k}\cdot\mathbf{r}_j}|a\rangle}{E_a - E_c + \hbar\omega_{\mathbf{k}} - i\Gamma_c/2}\right) \tag{3.10}$$

where m is the electron mass, E_a and E_c are the energies of the initial and intermediate states $|a\rangle$ and $|c\rangle$ respectively ($|b\rangle$ is the final state), $\hbar\omega_{\mathbf{k}}$ is the photon energy, $\mathbf{s}_j$ and $\mathbf{p}_j$ are the spin and momentum operators of the jth electron at site $\mathbf{r}_j$ and Γ is the core-hole lifetime of $|c\rangle$. Resonant elastic x-ray scattering corresponds to the case when $|a\rangle \equiv |b\rangle$ ($\hbar\omega_{\mathbf{k}} = \hbar\omega'_{\mathbf{k}}$).

Eq. 3.10 has an explicit dependence of the spins, however, for typical core level energies the dominant term is $\boldsymbol{\epsilon}\cdot\mathbf{p}$ [37]. Thus, Eq. 3.10 can be simplified into

$$\mathcal{A}_{res} \approx -\frac{1}{m}\sum_{c}\sum_{ij}\frac{E_a - E_c}{\hbar\omega_{\mathbf{k}}}\left(\frac{\langle b|(\boldsymbol{\epsilon}'\cdot\mathbf{p}_i e^{-i\mathbf{k}'\cdot\mathbf{r}_i}|c\rangle\langle c|(\boldsymbol{\epsilon}\cdot\mathbf{p}_j e^{i\mathbf{k}\cdot\mathbf{r}_j}|a\rangle}{E_a - E_c + \hbar\omega_{\mathbf{k}} - i\Gamma_c/2}\right) \tag{3.11}$$

and consequently the direct dependence on the spins is lost. The sensitivity to the magnetic degrees of freedom is instead achieved indirectly through the Pauli exclusion principle and SOC. Due to the Pauli principle, two electrons with parallel spin in different d orbitals will on average be further apart than two electrons with antiparallel spins (in the

same or different d orbitals). This reduces the Coulomb repulsion between the electrons and is therefore energetically favourable. The energy difference between the parallel and antiparallel alignment is called the exchange energy and is ultimately the cause of atomic magnetism. In condensed matter, where electron bands are formed, the inter-atomic as well as the intra-atomic exchange between electrons lead to the spin polarized splitting of the valence band. This exchange splitting (see Figure 3.4) results in an unequal number of unoccupied spin up and spin down states above the Fermi energy. Since the spin is conserved in optical transitions, core electrons with the same spin as the unoccupied intermediate state will have a higher probability of being excited. This discrepancy in the number of unoccupied states translates into non equal matrix elements (F_{11} and $F_{1\bar{1}}$) from Eq. 3.2 and 3.4 which leads to a non-vanishing resonant scattering amplitude. In the case of an equal amount of spin up and down states, the resonant magnetic scattering amplitude would be zero.

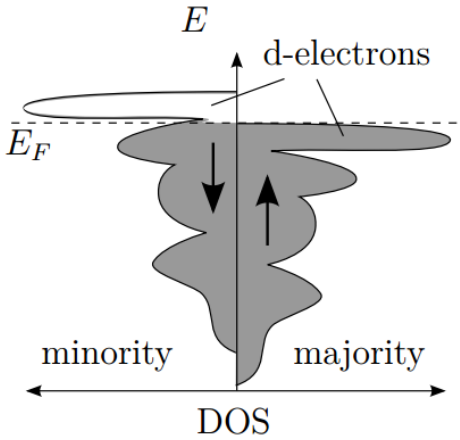

Figure 3.4: Schematic figure of the density of states (DOS) of the up and down spin states in a transition metal. The spin up state has lower energy than the spin down state which causes a discrepancy in the amount of unoccupied states above the Fermi energy. Figure obtained from [38].

In short, one can say that the non-resonant magnetic scattering process is due to the interaction between the magnetic field of the electromagnetic wave and the magnetic moments of the electrons. This interaction is due to small relativistic effects that were first studied by de Bergevin and Brundel [39, 40]. The XRMS process, however, can be though of as a more indirect probe of the magnetic structure through electronic excitations from spin polarized ground states.

3.3 Structure factor and magnetic structure

The final step in deducing the magnetic structure is realized by employing a structure factor calculation that relates the magnetic structure to Bragg intensities. Initially, the atomic structure factor will be considered, which can be derived to be [30]

$$\mathcal{F}_A = \sum_j f_j e^{2\pi i \mathbf{K}\cdot\mathbf{r}_j} \tag{3.12}$$

where $\mathbf{K}$ is the Miller index of the Bragg reflection of interest, $\mathbf{r}_j$ is a vector that specifies the position of the jth atom in Cartesian coordinates and f_j is the atomic form factor,

which is the Fourier transform of the electron density of the jth atom. This form factor represents the fact that the x-ray scattering intensity depends on the number of electrons in the atoms. In contrast, the magnetic scattering intensity depends on the size and direction of the spins as well as the strength of the transition that is probed (in this case an E1 (electric dipole) transition). The atomic form factor f_j therefore has to be replaced by the magnetic scattering strength $\mathcal{A}_{j,\mathrm{E1}}^{\mathrm{XRMS}}$ which takes these matters into consideration. The magnetic structure factor then becomes

$$\mathcal{F}_M = \sum_j \mathcal{A}_{j,\mathrm{E1}}^{\mathrm{XRMS}} e^{2\pi i \mathbf{K}\cdot\mathbf{r}_j}. \tag{3.13}$$

In the case of SIO, the spins are all of equal magnitude. Combining this with the fact that we are only studying the L_3 edge, $\mathcal{A}_{j,\mathrm{E1}}^{\mathrm{XRMS}}$ can (for now) be regarded as only containing the spin orientations.

As a first ansatz of determining the magnetic structure of our films, $\mathcal{F}_M$ is calculated using the previously determined magnetic structure of bulk SIO. If the magnetic structure of our films is indeed similar to that of bulk samples, the experimental results should conform with these calculations. The magnetic structure of bulk SIO is illustrated in Figure 3.5. The magnetic moments of the unit cell are numbered from 1 to 8, where moment 1 is placed at the origin. The vector $\mathbf{r}_j$ points to moment j from the origin and the moments themselves are defined by $[a, b, c]$. As an example, the position vector of moment number 2 is $\mathbf{r}_2 = [1/2, 1/2, 0]$ and its magnetic moment vector (since we are only considering the direction of the spins) is $\mathcal{A}_{2,\mathrm{E1}}^{\mathrm{XRMS}} = \widehat{\mathbf{z}}_2 = [-cos(\phi), -sin(\phi), 0]$. A calculation of $\mathcal{F}_M$ (Eq. 3.13) for this magnetic structure suggests that all the $(1\,0\,4n)$, $(1\,0\,4n+2)$ and $(0\,0\,2n+1)$ reflections are allowed and should yield finite intensities (the $(1\,0\,4n+2)$ Bragg peaks will however be ignored throughout the rest of this thesis). It should be mentioned that these reflections are not allowed according to the atomic structure factor calculation $\mathcal{F}_A$ (Eq. 3.12). This result is of great significance and will be revisited in Chapter 4. Note that the canting of the magnetic moments produces a $(\downarrow\uparrow\uparrow\downarrow)$ antiferromagnetic pattern along the c-axis with a ferromagnetic component in the ab-planes.

Performing the magnetic structure factor calculation on a system where $\phi = 0°$ and the magnetic moments pointing along the a-axis we find that the $(1\,0\,4n)$ is allowed while $(0\,0\,2n+1)$ is not. On the other hand, if the magnetic moments point along the b-axis (as if the canting angle was $\phi = 90°$) we instead find that $(0\,0\,2n+1)$ is allowed and $(1\,0\,4n)$ is forbidden. Thus, the $(1\,0\,4n)$ and the $(0\,0\,2n+1)$ peaks probe the magnetic moments along the a- and b-axis respectively. This result is important, as no matter what angle of ψ (see Figure 3.3) the sample is put at, a response from the b-axis will never be observed while studying the $(1\,0\,4n)$ reflections. The opposite is true for the $(0\,0\,2n+1)$ reflections.

The magnitude of the canting angle is estimated by comparing observed and calculated relative intensities of the two different sets of Bragg peaks. For a canting angle of $\phi = 12°$ the relative intensity is $I_{(1\,0\,4n)}/I_{(0\,0\,2n+1)} \approx 45$ according to calculation. This is the expected observed ratio if the magnetic structure of our films is identical to that of bulk SIO.

The task of this thesis was not only to determine the magnetic structure of the SIO films but also to determine how it changes under the influence of a magnetic field and temperature. When the sample is heated, thermal fluctuations prohibit the magnetic moments from retaining their orientation. This loss in order will ultimately result in the quenching of the magnetic Bragg peaks and we should therefore expect to see a decrease

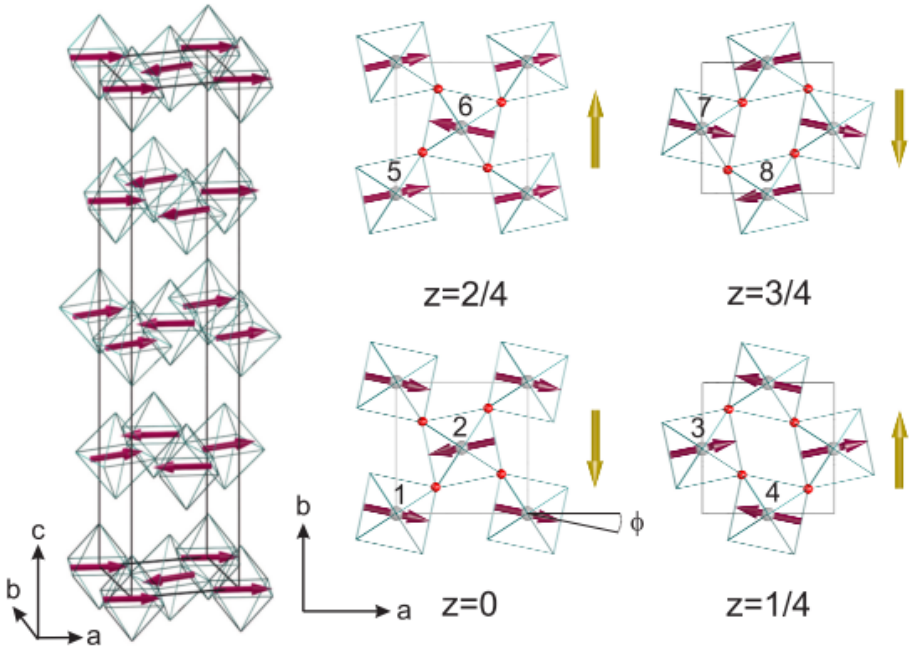

Figure 3.5: The magnetic structure of SIO, ϕ is the canting angle of the spins. The net magnetic moments along the b axis are represented by the yellow arrows, producing a ferromagnetic component in the ab-planes with an antiferromagnetic ($\downarrow\uparrow\uparrow\downarrow$) pattern along the c axis. Figure obtained from [4].

in intensity as the temperature is increased. At a critical temperature T_N, the Néel temperature, all magnetism is lost. An applied magnetic field should also affect the magnetic structure as the spins would favour to align with the field. Previous measurements [11] suggest that an externally applied magnetic field (~ 300 mT) alters the magnetic structure from an antiferromagnetic to a ferromagnetic along the c-axis (see Figure 3.6) through the 180° flip of some magnetic moments. If $\mathcal{F}_M$ is calculated for this new magnetic structure one finds that the $(1\,0\,4n)$ and $(0\,0\,2n+1)$ Bragg peaks are no longer allowed and replaced by $(0\,1\,2n+1)$. This is another important result that will be recalled in Chapter 4.

In these calculations only the spin orientations were considered; in reality the magnetic scattering strength is also dependent on the overlap of the x-rays electric vector with the magnetic moments. Still neglecting the transition probability, the magnetic scattering strength for the moments along the a- and b-axis can be written for the two different sets of reflections as [4]

$$\mathcal{A}^{\mathrm{XRMS}}_{j,\mathrm{E1}_{a,(104n)}} \propto i\hat{\mathbf{z}}_j \cos\phi(\cos\chi\cos\theta\cos\psi + \sin\theta\sin\chi) \tag{3.14}$$

and

$$\mathcal{A}^{\mathrm{XRMS}}_{j,\mathrm{E1}_{b,(002n+1)}} \propto i\hat{\mathbf{z}}_j \sin\phi\sin\psi\cos\theta \tag{3.15}$$

respectively, where θ is the Bragg angle, ψ is the azimuthal angle around the scattering vector $\mathcal{Q}$ and χ is the angle between $\mathcal{Q}$ and the c-axis (see Figure 3.3). These equations allow us to calculate the intensity as the sample is rotated around ψ in a so called azimuthal dependence, using

$$\mathcal{I} \propto \left| \sum_j e^{2\pi i \mathbf{K}\cdot\mathbf{r}_j} \mathcal{A}^{\mathrm{XRMS}}_{j,\mathrm{E1}} \right|^2 . \tag{3.16}$$

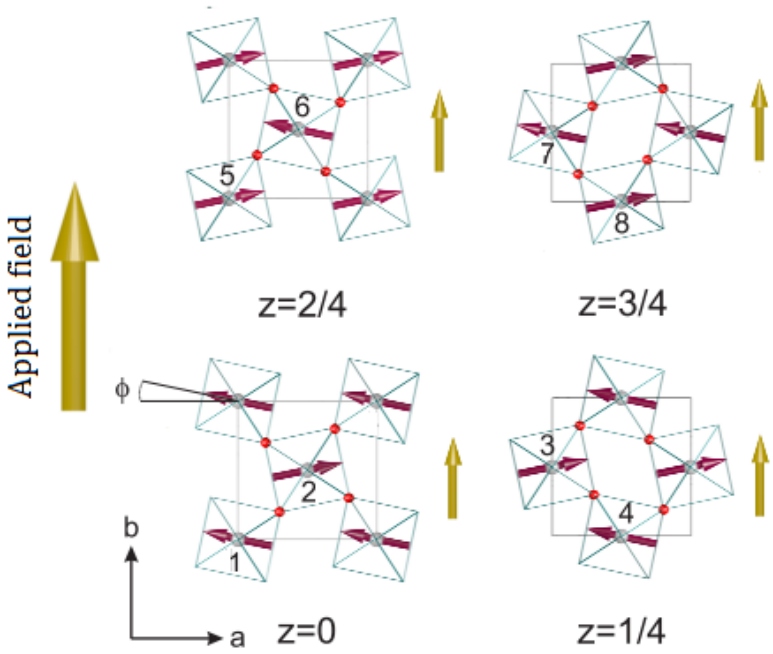

Figure 3.6: An externally applied magnetic field alters the spin orientations and produces a ferromagnetic stacking along the c-axis. Adaptation of Figure 3.5.

In this calculation θ and χ are assumed to be constant under rotation of ψ, furthermore χ is assumed to be close to zero (which it was in the experiments). By rotating ψ the overlap between the electric field vector and the magnetic moments is altered. The calculated azimuthal dependence for the $(1\,0\,4n)$ and the $(0\,0\,2n+1)$ reflections in zero field, as well as the in-field $(0\,1\,2n+1)$ reflections (Eq. 3.14 was used for $(0\,1\,2n+1)$) is illustrated in Figure 3.7. The dominant component of the spins are parallel with the a-axis and thus maximum response for both $(1\,0\,4n)$ and $(0\,1\,2n+1)$ is obtained at corresponding angles. The $(0\,0\,2n+1)$ reflections probe the b component of the spins and is thus much weaker and antiphased with respect to the other two sets of reflections.

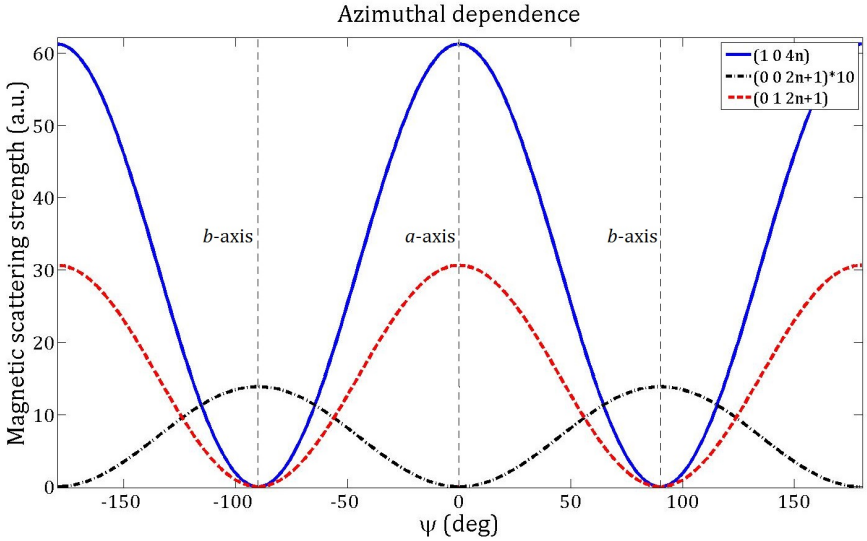

Figure 3.7: Calculated azimuthal dependence of three different types Bragg reflections. Note that $(0\,0\,2n+1)$ has been scaled by 10.

Chapter 4

Experimental Results

This chapter presents how XRMS has been used to determine the magnetic structure of the SIO films. All diffraction peaks have been fitted with Lorentzian functions which have then been analysed in different ways. Analytical integration of the Lorentzian fits were made to estimate the integrated intensity. This is a good estimate of the total scattering since it takes both the peak height and the width into account, in contrast to just using the peak intensity. A Lorentzian function was chosen as it provides a good model of the experimental data to eye and no particular physical interpretation was used. The experimental results will merely be stated with minimal discussion in the initial sections of this chapter, the results are instead discussed in the final section.

4.1 XRMS energy dependence

The structure factor calculation from Section 3.3 determined that magnetic structural peaks should appear at $(1\,0\,4n)$ and $(0\,0\,2n+1)$ for the known bulk magnetic structure of Figure 3.5. It also shows that the crystal structure will not produce any peaks at these Bragg reflections. Naturally the first task was to try and find these peaks in our films to determine if they have the same magnetic structure as the bulk compound. The large c-lattice parameter of 25.7 Å results in inconveniently low grazing angles for small n and although some of these peaks were found, they were not further investigated for this reason. The following measurements will focus on higher order reflections such as the $(1\,0\,20)$, $(0\,0\,19)$ and the $(0\,1\,19)$ reflections. The first thing to mention here is that reflections corresponding to $(0\,0\,2n+1)$ such as $(0\,0\,19)$ were not observed despite systematic search below T_N. This peak corresponds to the small component of the magnetic moment along the b-axis due to the canting of the spins shown in Figure 3.5. The fact that we could not find it could mean two different things, either the canting angle is approaching zero, or our beamline simply did not provide sufficient sensitivity for the weak scattering from the small spin canting. The expected intensity ratio is $I_{(0\,0\,19)}/I_{(1\,0\,20)} \approx 1/45$ for a canting angle of 12° according to our structure factor calculations. However we did succeed in observing peaks corresponding to $(1\,0\,4n)$ in thick 120 nm films, suggesting that the magnetic structure is similar to the bulk.

The next step was to tune the photon energy to overlap with the transition from the $2p$ state to the $j_{\text{eff}} = 1/2$ state (the L_3 edge) in SIO as mentioned in Section 3.2. The performed energy scan (Figure 4.1) serves two purposes. The fact that the $(1\,0\,20)$ reflection was found at 11.22 keV (similar to 11.217 keV as observed by [4], the small difference is likely due to energy calibration of beamlines) is a first indication of our

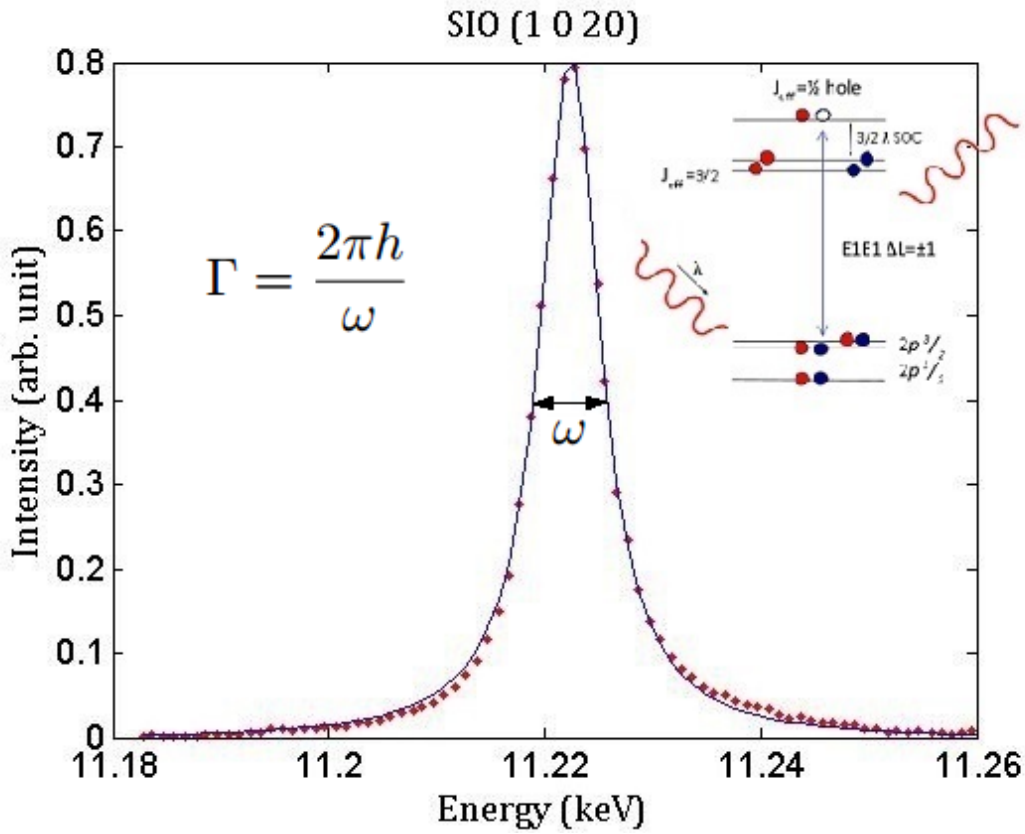

Figure 4.1: Bragg peak (1 0 20) with Lorentzian fit. The core-hole lifetime can be estimated by the FWHM to be ~ 3.7 fs. Inset is a modification of Figure 3.2.

magnetic structure being similar to bulk SIO. Secondly, it served as an energy calibration curve and the photon energy corresponding to the peak intensity was used throughout the rest of the experiments. The core-hole lifetime Γ of the $j_{\text{eff}} = 1/2$ state can be estimated using the equation in Figure 4.1, where h is Planck's constant and ω is the full width at half maximum (FWHM), this results in $\Gamma \approx 3.7$ fs.

Although these results seem promising, we cannot yet exclusively conclude that we observe magnetic scattering. In principle these (1 0 20) peaks could still be Thomson scattering arising from an unexpected crystal structure. This is especially true in thin film research, where small non-stoichiometric impurities could be present. In order to exclusively dismiss this possibility, the polarization of the scattered waves was analysed.

4.2 XRMS polarization dependence

As mentioned in Section 3.2, E1 XRMS in our scattering geometry with incident σ-polarized light changes the state of polarization of the scattered wave, whereas Thomson scattering does not. If the (1 0 20) Bragg peak is produced by XRMS we expect to see a change in polarization after the scattering process. In this experiment, the incoming waves were always σ polarized and the polarization analyser of the beamline was used to determine if the final waves were σ or π polarized. The results shown in Figure 4.2 are clearly not consistent with Thomson scattering since the polarization has indeed changed from σ to π (however there is some cross contamination). From this analysis it is quite apparent that (1 0 20) peak truly is the result of XRMS probing the $j_{\text{eff}} = 1/2$ state in

our film.

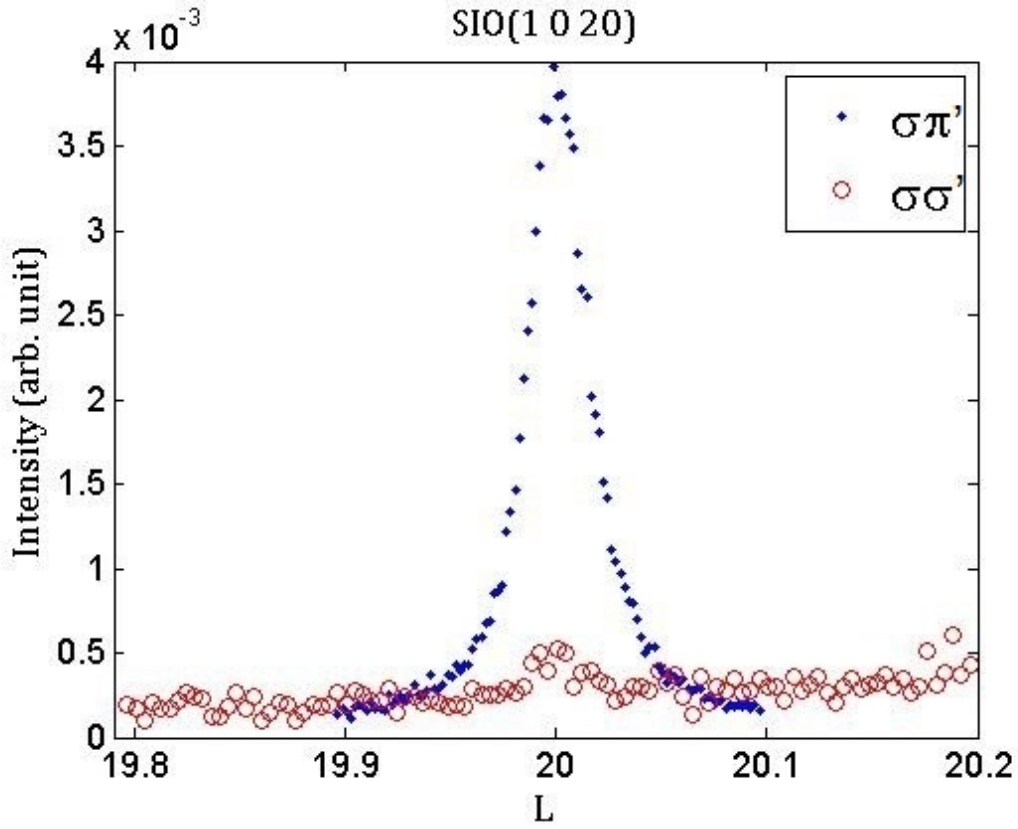

Figure 4.2: Measured intensity for the two orthogonal polarization states. Note the small signal obtained in the $\sigma\sigma'$ channel due to cross contamination, as explained in Section 2.3.1.

4.3 XRMS azimuthal dependence

An azimuthal dependence of the (1 0 20) reflection was then carried out to determine the orientation of the magnetic moments. In this experiment the sample was rotated 180° around the scattering vector of (1 0 20) (see Figure 3.3) and the scattered intensity measured in steps of 10°. Recalling the structure factor calculation in Section 3.3, different Bragg reflections probe different components of the magnetic moments and $(1\,0\,20)\mu \parallel a$ while $(0\,0\,19)\mu \parallel b$. The results seen in Figure 4.3 thus imply that the dominant magnetic component points along the a-axis since the film is rotated 45° with respect to the substrate as explained in Chapter 2.

The fact that the response seems to go to zero at −45° and 135° indicates that there is no (or an extremely tiny) component along the c-axis. The $\sigma\pi'$-channel of Eq. 3.9 contains a factor of z_3 (along the c-axis) which means that any magnetic component along the c-axis should be picked up as a response in this scattering geometry. This component should be independent under rotation of ψ and thus always give the same response. If the response goes to zero for any angle of ψ the component along c must also be zero. This result perfectly conforms with considerations from Section 3.3 (Figure 3.16) apart from the fact that (0 0 19) was never found.

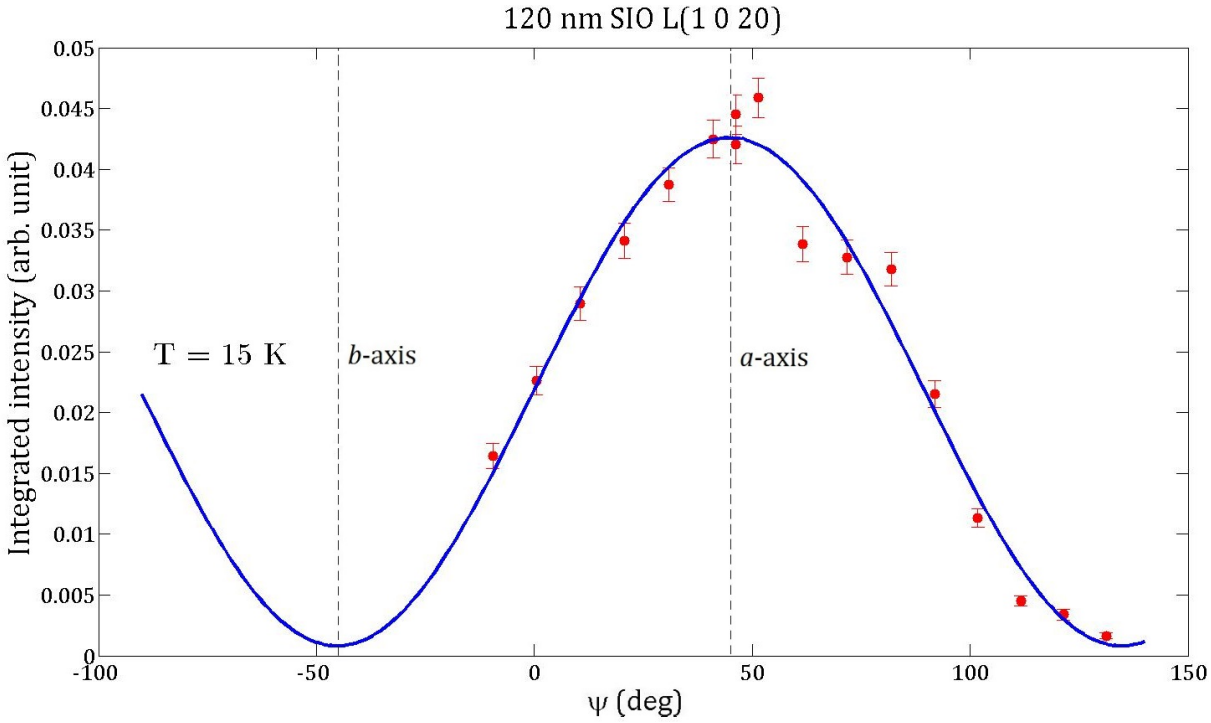

Figure 4.3: The azimuth dependence of (1 0 20). The data was fitted with Eq. 3.16. The function seems to go to zero at 135°and -45°suggesting that there is no spin component along the c-axis. Note that the fit has been extrapolated for negative angles of ψ.

4.4 XRMS temperature dependence

Having established the magnetic origin of the (1 0 20) reflection and the direction of the magnetic moments, we turned our attention to the temperature dependence. The (1 0 20) peak was studied as the temperature of the sample was increased from 10 K to 240 K as can be seen in Figure 4.4. When the temperature of a magnet is increased the magnetic structure is lost as explained in Section 3.3. This is seen as a drop in peak (integrated) intensity and an increase in FWHM in Figure 4.4. The thermal evolution of the magnetic scattering intensity is expected to vary according to $\mathcal{I} = A\left(\frac{T_N - T}{T_N}\right)^{2\beta}$ for temperatures above 110 K where β is a parameter that distinguishes continuous phase transitions, it is essentially a measure of the thermal evolution of the antiferromagnetic order, T_N is the Néel temperature when all magnetic order is lost and A is a constant.

The average values of T_N and β of the three different measurements (with miller indices H, K and L) were estimated from the fits to be 221 K and 0.36 respectively. The value of T_N is in agreement with bulk measurements [4] but the β order parameter is not. Previous measurements have determined β to be around 0.195 [41] and 0.23 [42]. The value of β has been predicted to be 0.3647 by the 3D Heisenberg model, 0.325 by the 3D Ising model and 0.346 by the 3D $X-Y$ model [43]. Furthermore, an exact solution for 2D systems only exists for the 2D Ising model which predicts a value of $\beta = 0.125$ [44], while for the 2D $X-Y$ and 2D Heisenberg models no long range order is expected at finite temperature [4]. There is however a report of there being 2D $X-Y$ systems with weak perpendicular coupling $J_\perp$ ($J_\parallel/J_\perp \sim 10^3 - 10^4$) with $\beta = 0.23$ [45]. The agreement of our observed β value with the 3D models is suggestive of our films being 3D magnets, whereas bulk SIO seems to behave more like 2D magnets. Due to the 3D shape of the $j_{\text{eff}} = 1/2$

wavefunction (see Figure 1.4) it should permit 3D-like interactions but due to the large interlayer spacing of 25.7 Å it is reasonable to expect that the system might become a quasi-2D magnet, as seems to be the case of bulk SIO [4]. The interaction between the magnetic moments along the three different axes can be determined by estimating FWHM of the Bragg peaks. The correlation length, which is the distance over which the spins are correlated is

$$L_C = \frac{d}{\pi\omega} \tag{4.1}$$

where ω is the FWHM and d is the lattice spacing in the given direction. One can see from the bottom part of Figure 4.4 that the FWHM for H and K is about 4 times smaller than for L. This is expected as the L scans corresponds to the c lattice parameter which is a lot larger than a and b. Using Eq. 4.1 one finds that the correlation length is ~ 20 Å along all three crystallographic axes. This corresponds to roughly one unit cell along c but about four along a and b. Thus, it seems to be equally correlated in all directions, which is consistent with a 3D-like behaviour.

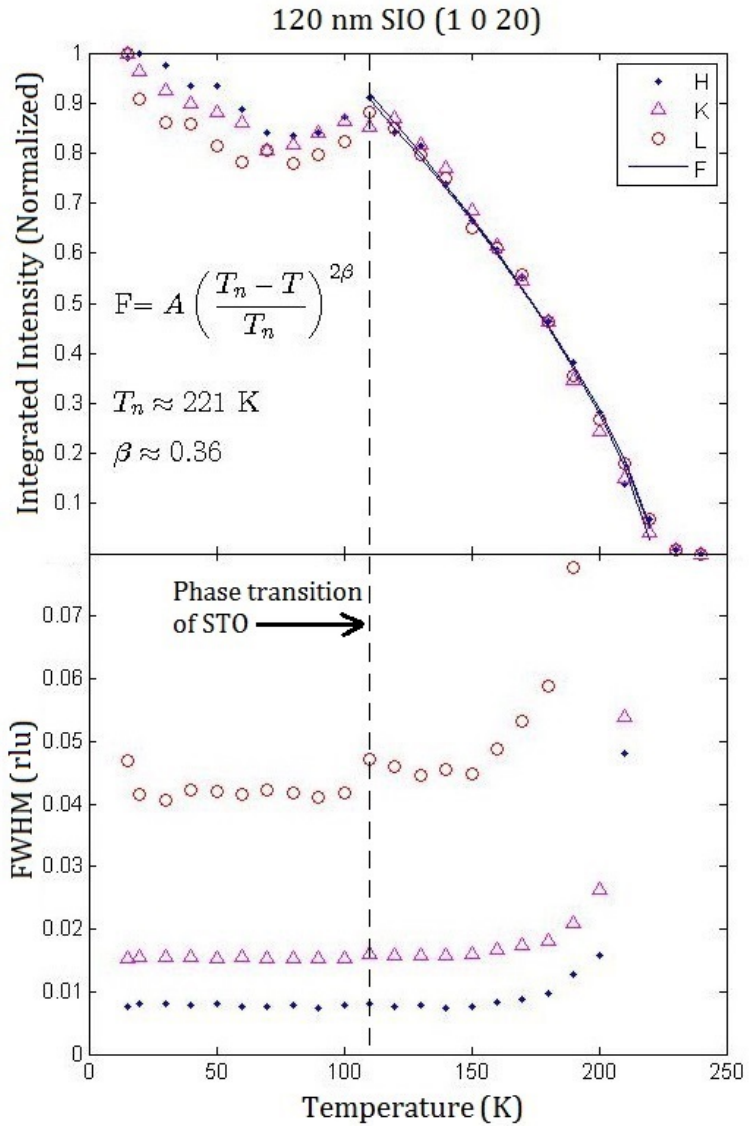

Figure 4.4: (Top) Temperature dependence of the (1 0 20) reflection in SIO. The solid line is a fit to the power law F. (Bottom) The FWHM of the peaks vs. temperature.

4.5 XRMS with applied magnetic field

The magnetization response as a function of temperature of the film (Figure 4.5) has previously been measured by Stephan Geprägs in a SQUID magnetometer (superconducting quantum interference device). The magnetization response is a great deal larger when a field is applied than in zero field. This could be a first indication of canted spins since this type of response usually is associated with ferromagnetism. However, this ferromagnetic response is not exclusive of a canted magnetic structure. In principle it could arise from any type of ferromagnetic structure (an unwanted metal impurity for instance). This section will present further investigations of the film under the influence of magnetic fields.

One can see a sudden change in both of graphs of Figure 4.5 at the phase transition of the STO substrate (110 K). For the measurement in zero field the magnetization suddenly increases below 110 K whereas it decreases when a field is applied. This phenomenon has been further investigated and a hysteresis effect was observed that disappeared close to this temperature. This can be seen in Figure 4.9 and 4.10. Another noticeable difference is that T_N seems to have been shifted to a higher temperature when the field was applied.

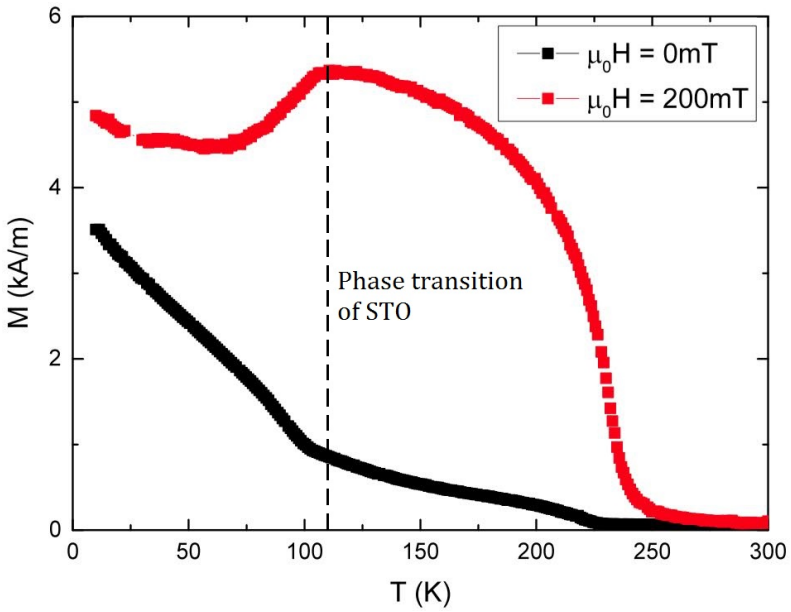

Figure 4.5: Magnetization measured with a SQUID. Note the sudden change in response at around 110 K due to the phase transition of the STO substrate.

In the experiments performed in this thesis, a magnetic field was applied along the b-axis of the sample (see Figure 2.8 and 3.5). In bulk SIO this altered the spin orientations as shown in Figure 3.6. According to calculation (Section 3.3) the (1 0 20) Bragg peak should be forbidden for this structure while (1 0 19) and (0 1 19) instead are allowed. This is precisely what was observed and another noticeable effect of the applied field is the massive broadening of the L peaks as seen in Figure 4.6. The correlation length in the c-direction is thus greatly reduced when the field is applied. Calculating the correlation length (Eq. 4.1) one finds it has been reduced from ~ 20 to ~ 3 Å in the c direction while it has stayed the same in a and b.

An azimuthal dependence was also performed in a magnetic field of 200 mT. As seen in Figure 4.7 the behaviour has not changed and the dominant component of the spins are still along the a-axis. These results agree well with calculations in Section 3.3 and tells

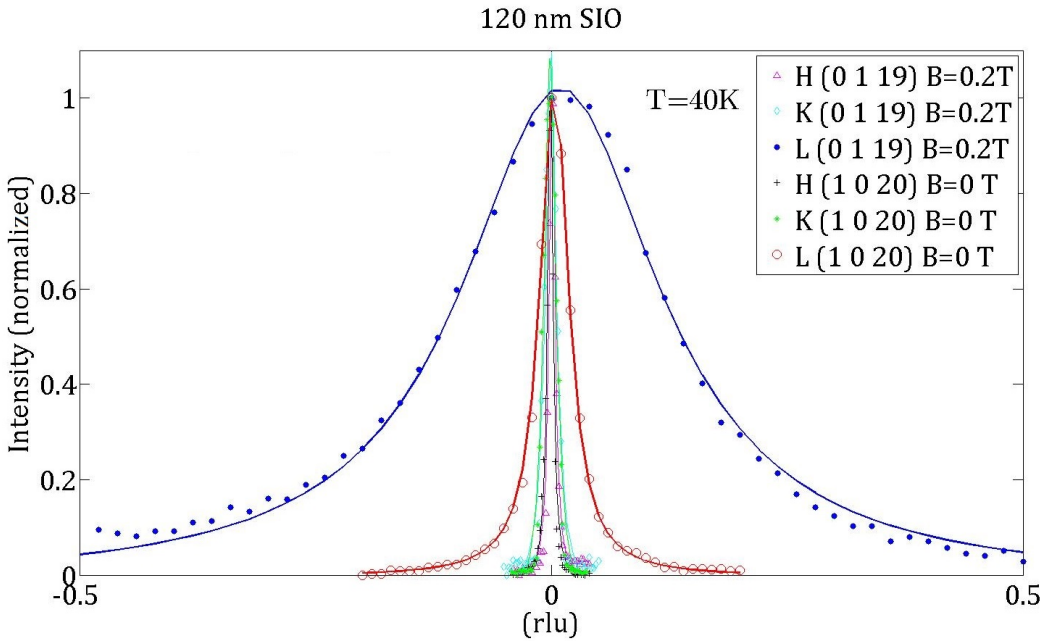

Figure 4.6: The broadening of an L peak under the influence of an applied magnetic field.

us that the applied magnetic field does not change the magnetic structure in a significant way, apart from the 180° flipping of the spins. This is expected if the magnetic structure of our film indeed changed to that of Figure 3.6 under the influence of an applied field. These results support the possibility of canting but does not directly deduce this scenario. Interestingly, the intensity is higher for the (1 0 19) and (0 1 19) peaks than for the (1 0 20); which disagrees with previous calculations (see Figure 3.7) and will be discussed further in Section 4.6. Most important however, is the fact that the phase of the azimuthal dependence has been retained under the effect of an applied field.

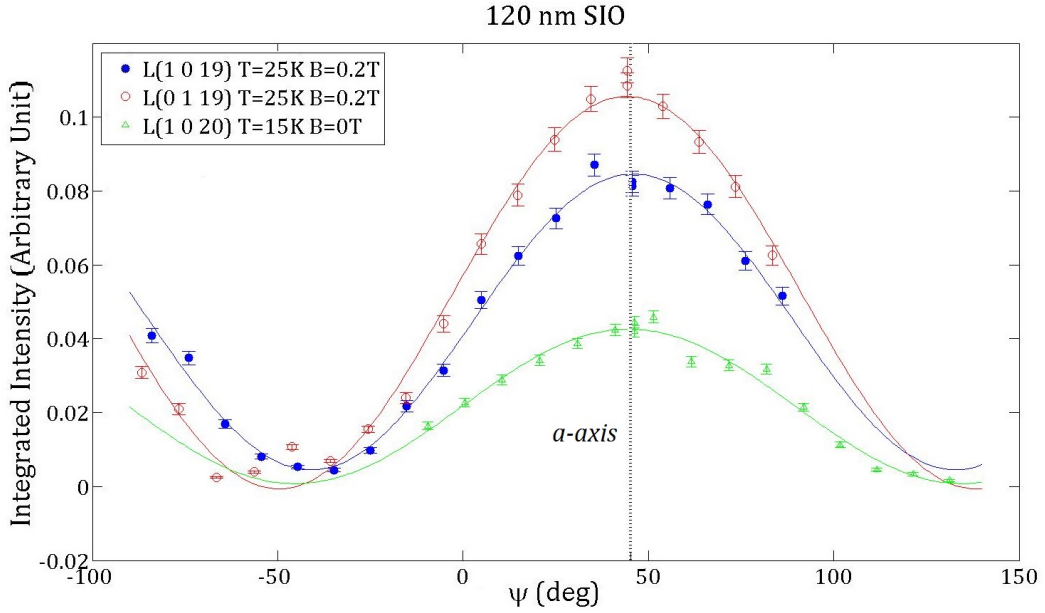

Figure 4.7: In-field azimuth dependence compared with zero-field. The data has been fitted with Eq. 3.16.

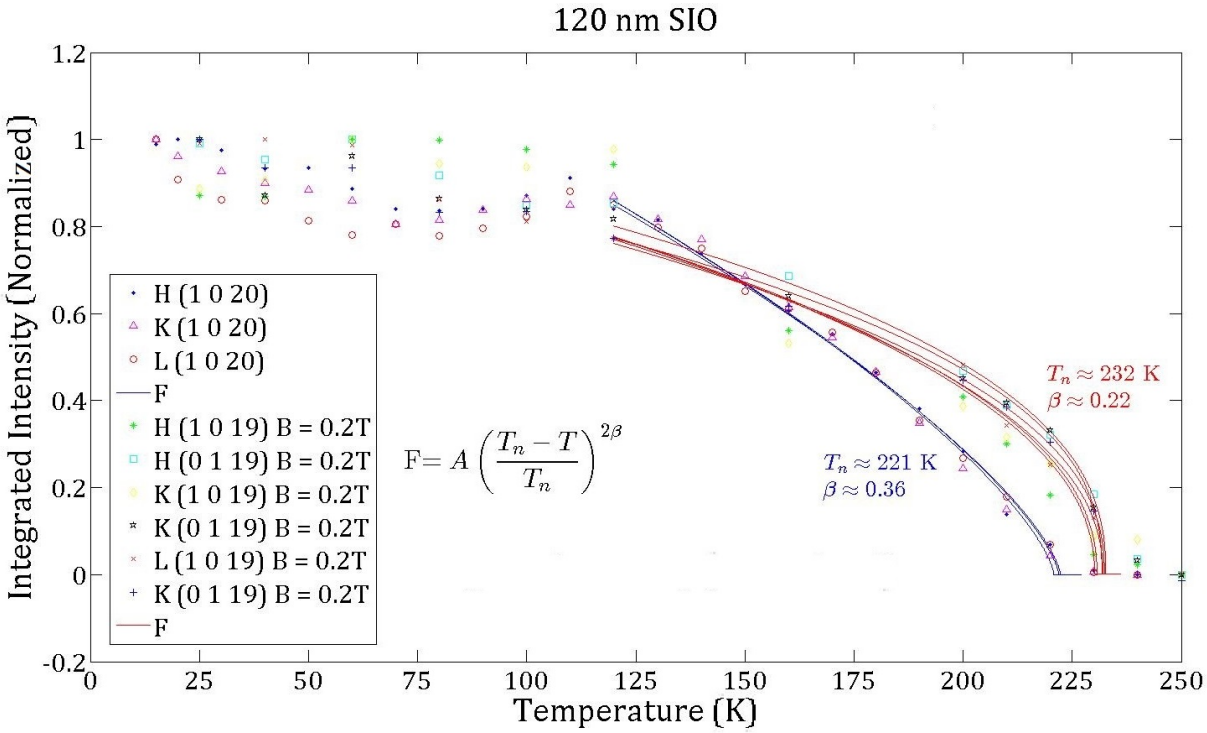

Figure 4.8: Temperature dependence of (1 0 20) in zero field compared with (0 1 19) in field. The solid lines are fits to the power law F. The zero-field data has been fitted with blue curves and the in-field data has been fitted with red curves. The displayed values of T_n and β are the average values from the two sets of fits.

The next measurement was a temperature dependence in the applied magnetic field. The results can be seen in Figure 4.8 where they are compared with the results obtained in zero field (Figure 4.4). Just as in the magnetization measurement (Figure 4.5) T_N has been shifted to slightly higher temperatures. Furthermore, β has changed from ~ 0.36 to ~ 0.22 which seems to suggest that the system has become more like a 2D magnet with weaker interactions in one spatial dimension. This result agrees with the decreased correlation length in the c-direction which is seen as the broadening of the L peak in Figure 4.6.

Finally, the intensity of the (1 0 20) and (0 1 19) (because the large magnet seen in Figure 2.8 blocked the scattered beam at certain angles we were forced to study (0 $\bar{1}$ 20) and (0 $\bar{1}$ 19) instead) was measured in a varying magnetic field for a few different temperatures (see Figure 4.10). A hysteresis effect for low temperatures was observed that disappeared close to the phase transition of STO (110 K). The distance between the hysteresis peaks was plotted as a function of temperature and it seems to return a linear relationship. The distance completely vanishes close to the phase transition of STO (110 K), this can be seen in Figure 4.9.

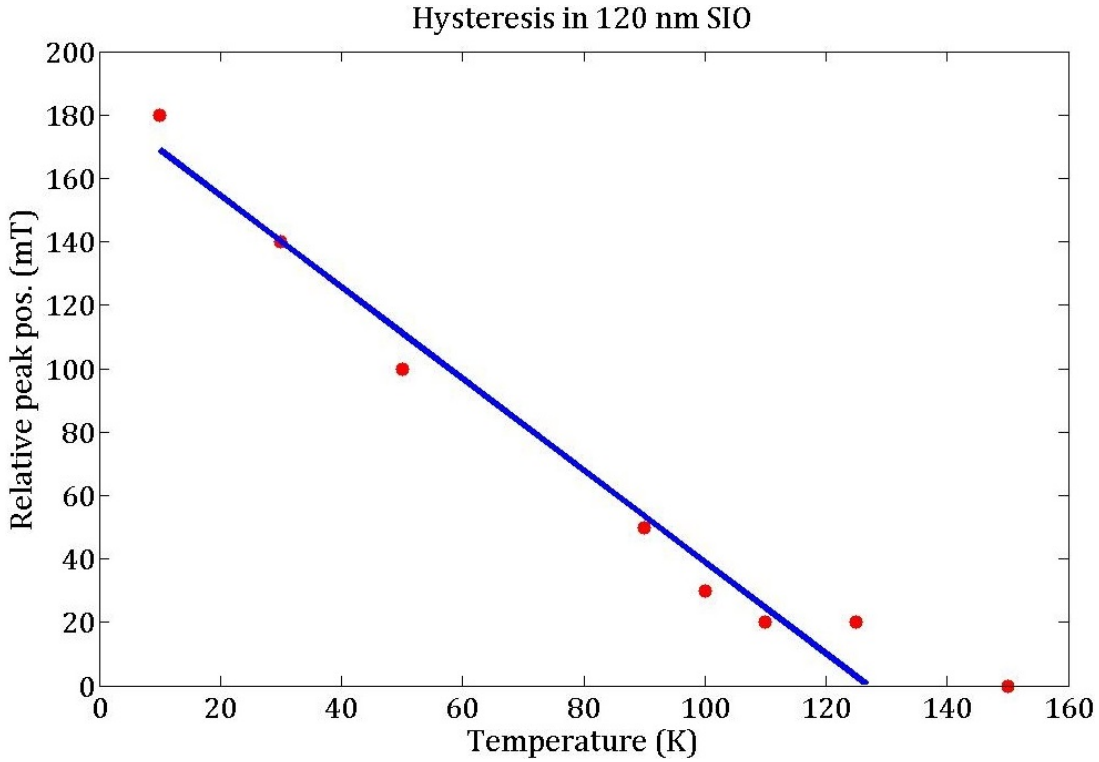

Figure 4.9: Temperature dependent hysteresis effect. The peak positions were estimated simply by the peak extremum of the data points in Figure 4.10.

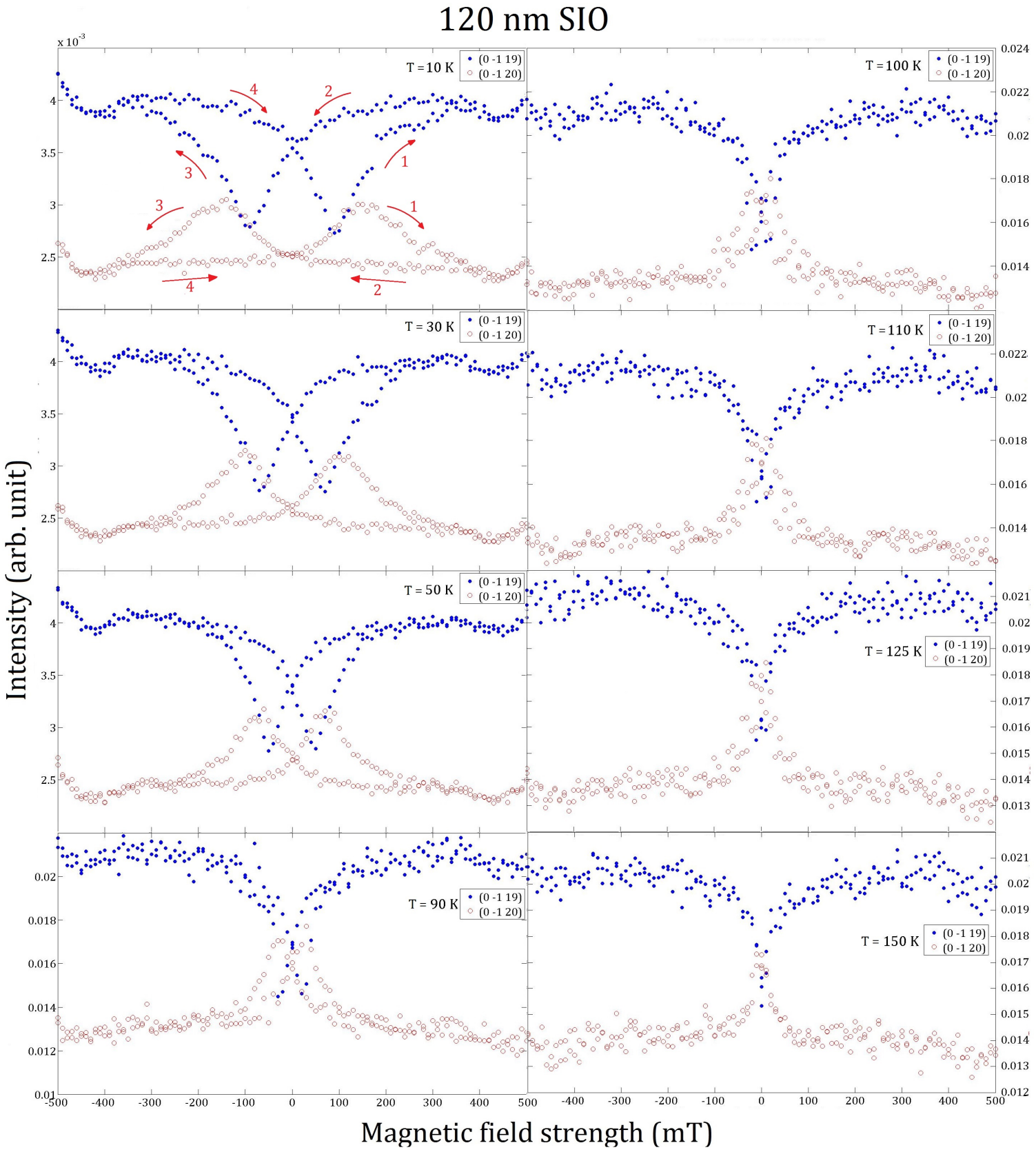

Figure 4.10: The hysteresis effect at a few different temperatures. The magnetic field was varied from 0 mT → 500 mT → -500 mT → 0 mT. The red arrows in the top of the figure illustrate the path of the hysteresis loop. The different intensity scales are due to a normalization problem, in reality they are of the same magnitude.

4.6 Discussion of results

The results from the energy dependence and the polarization dependence together convincingly demonstrated that we indeed were probing the magnetic $j_{\text{eff}} = 1/2$ state in a crystal with an antiferromagnetic structure similar to that of bulk SIO. The reasons for this were triplicate. First, the atomic structure factor calculation suggested we should not find a Bragg peak at (1 0 20) whereas the magnetic structure factor calculation did. Second, the peak we found closely conforms with the precise energy of the L_3 transition. Third, the state of polarization was changed in the scattering process which is not consistent with Thomson scattering, it is however consistent with XRMS in our scattering geometry.

So far it seems the structure of our 120 nm SIO film is identical to that of bulk SIO, however one crucial difference is that we could not find the (0 0 19) Bragg peak. Other studies [4] have found this peak using a high flux undulator beamline at Diamond Light Source. Without the observation of this peak we have no direct evidence that the magnetic moments in our films are canted. However, we can still put forth some strong arguments for the case through the rich contents of our experiments.

The magnetic structure factor calculation of a structure similar to that of bulk SIO (Figure 3.5) but with a canting angle $\phi = 0°$ suggests the (1 0 20) reflection is allowed. It does not however, allow the (0 1 19) reflection. The change in the magnetic structure from Figure 3.5 to 3.6 when a field is applied relies on the canting of the spins. This means that the structure of a non-canted system should not change under the effect of an externally applied (modest) magnetic field. The crucial point of the argument is that the (1 0 20) peak disappeared and the (0 1 19) peak was found when the field was applied, a peak that according to the magnetic structure calculation should be forbidden for the non-canted system. Evidently something changed when the field was applied, and it changed in a way that perfectly (apart from the intensity) agrees with calculations on the canted system.

If one compares Figure 3.7 with Figure 4.7 one can see that according to calculation the intensity of the (0 1 19) should be half that of (1 0 20). The experiments show quite the opposite however. This might be explained by considering two different domains, A and B, where the dominant spin component points along the a- and b-axis respectively. In the zero-field experiment we are only probing domain A, but the effect of the magnetic field might align the ferromagnetic component of these domains such that only one large domain is obtained. Effectively the B domain would switch over and become part of the A domain. The measured intensity should thus be increased. This argument alone would suggest the ratio between A and B before the applied field was $A/B \approx 1/4$ since the observed change in intensity was ~ 4 times higher than expected (in the calculation only one domain was considered). However the intensity might be affected by other factors as well.

The other major disparity between SIO in bulk and in films is the temperature evolution of the systems. Our observed β value suggests the films behave like 3D magnets, while bulk SIO seems to behave more like 2D. Furthermore, the effect of an applied field along the b-axis seemed to transform our films into a 2D system. As previously mentioned, the topology of the $j_{\text{eff}} = 1/2$ wavefunction should not favour interaction along a certain crystallographic axis. However, the lattice parameter of the c-axis is about 4.7 times as large as the a- and b-axes and it is thus reasonable to expect less interaction in this direction. Interestingly, the FWHM for the L scans are $\sim 3 - 5$ times as high as for the H and K scans, resulting in similar correlation length along the three crystallographic

axes. It is not yet fully understood why our films seem to behave like 3D magnets in zero field while bulk samples seem to be more 2D-like. It might have to do with the clamping of the film on the substrate which could be verified by trying other substrates.

The applied magnetic field that transforms our 3D system to a 2D system somehow cuts the interaction along the c-axis. This also agrees with the L peaks becoming enormously broad when the field is applied. Exactly why the magnetic field decreases the interaction only along the c-axis is not yet fully understood.

As a speculation, the $j_{\text{eff}} = 1/2$ wavefunction seems to becomes a bit "squashed" in the c-direction under the influence of the field, prohibiting interaction. There is however no apparent reason why this squashing should only occur in the c-direction. It should, if not in all directions, be squashed in all directions perpendicular to the applied field, due to cylindrical symmetry around the axis of the field. If the field is imagined to only slightly "squeeze" the wavefunction in the directions perpendicular to the applied field, it might have significantly different consequences for the interaction along a and c. If the wavefunctions barely overlap with adjacent ligands in the c-direction, a slight diminution of the wavefunction should be fatal to the interaction in this direction. In the a-direction however, where the correlation length is over several lattice units, the effect might not be significant. Even if the wavefunction is squashed by the magnetic field in all three directions it would still only significantly change the interaction along c according to this argument. It would be interesting to see what would happen if the field was applied along the c-axis. Perhaps in this case the correlation length along c would remain the same, however this was never tested due to lack of time.

A subtle, yet noticeable effect of the magnetic field is that T_N is shifted to slightly higher temperatures when the field is applied. This was observed in both the magnetization graph (Figure 4.5) and in the in-field temperature dependence (Figure 4.8). This could be interpreted as the field "locking" the spins in place since they prefer to align with the field. When the temperature is increased to a point where the spins cannot retain their orientation the magnetic order is lost. If the applied field makes the spins more resistant to thermal fluctuations then naturally more energy is required to perturb them.

As discussed above, the magnetic structure is most likely canted with a ferromagnetic component. Thus, it is not completely unreasonable to find a hysteresis effect in the sample as it is common for ferromagnets. It should be noted that we did not measure the magnetization of the sample, we probed the magnetic structure using diffraction. The usual hysteresis effect arises from the ability of magnetic domains to remember their orientation after an applied field has been removed. In this case, it is the spins that have been flipped 180° that retain their orientation. This is not necessarily expected because an antiferromagnetic ordering is normally favoured in this compound. However, it is not either completely unreasonable since ferromagnetic components generally like to align.

The most interesting phenomenon regarding the hysteresis effect was that it vanished close to the phase transition of the substrate. It is therefore likely that it is related to strain effects. Although, if this was the case, a sudden change in strain exerted by the substrate should result in a sudden change in the hysteresis effect. By inspecting the data of Figure 4.9 and 4.10 a sudden change at 110 K is not observed. Instead the hysteresis effect seems to decrease linearly irrespective of the phase transition. By close inspection, one may notice a small hysteresis effect even at 125 K, which is well above 110 K. Perhaps magnetic scans of the same film on a different substrate might resolve this issue.

Chapter 5

Outlook

The task of this thesis was to compare the magnetic structure of epitaxial Sr_2IrO_4 thin films with bulk samples and evaluating the effects of strain from the $SrTiO_3$ substrate. Furthermore, the behaviour under the influence of an applied magnetic fields and temperature was studied.

The magnetic structure of thick 120 nm SIO films seems to be identical to bulk. Although direct evidence of Bragg peaks related to the canting of the magnetic moments were not observed, detailed analysis of substantial amounts of data signified the presence of canted spins. Ironically, the thin films behaved like 3D-magnets (equal interaction in three directions) whereas bulk samples displayed a more of a 2D-like behaviour (diminished interaction along the c-axis). The effect of an applied magnetic field distinctly changed the films into 2D magnets. A novel temperature dependent hysteresis effect was observed in the films, possibly an effect of strain. Numerous questions raised in this thesis remain unanswered; more measurements are required and some models should be tested to resolve these issues.

A proposal for beamtime at a higher flux undulator beamline at Diamond Light Source has been approved. Here, the 30 nm films will be studied again to see if any magnetic Bragg peaks can are observed. Furthermore, an attempt at detecting the weak (0 0 19) Bragg peak in the 120 nm SIO film will be made in order to directly determine if the spins are canted. Additional precise measurements should be carried out to more accurately estimate parameters like T_N and β, as well as the behaviour of the temperature dependent hysteresis effect. A 120 nm SIO film with a different substrate should be studied to determine if the 3D-like behaviour of our film was a consequence of strain, or merely a consequence of thickness. It should also be studied to deduce if the temperature dependent hysteresis effect was a result of strain or an intrinsic property of the film. Furthermore, the domain distribution will possibly be investigated as well as other films, such as $Sr_3Ir_2O_7$ with a larger c lattice parameter. If practically possible, it would be interesting to investigate the effect of an applied magnetic field along the c-axis. Lastly, it could be useful to study the crystal structure of the film and the substrate under the effect of a magnetic fields and temperature to see if the behaviour of the hysteresis effect conforms with a behaviour in the crystal structure of the film or the substrate.

Bibliography

[1] J George Bednorz and K Alex Müller. Possible high t c superconductivity in the ba—la—cu—o system. In *Ten Years of Superconductivity: 1980–1990*, pages 267–271. Springer, 1986.

[2] AP Ramirez. Colossal magnetoresistance. *Journal of Physics: Condensed Matter*, 9(39):8171, 1997.

[3] Sang-Wook Cheong and Maxim Mostovoy. Multiferroics: a magnetic twist for ferroelectricity. *Nature materials*, 6(1):13–20, 2007.

[4] Stefano Boseggia. *Magnetic order and excitations in perovskite iridates studied with resonant X-ray scattering techniques*. PhD thesis, UCL (University College London), July 2015.

[5] JP Clancy, N Chen, CY Kim, WF Chen, KW Plumb, BC Jeon, TW Noh, and Young-June Kim. Spin-orbit coupling in iridium-based 5 d compounds probed by x-ray absorption spectroscopy. *Physical Review B*, 86(19):195131, 2012.

[6] Andrei Tokmakoff. 5.74 introductory quantum mechanics ii, spring 2009.(massachusetts institute of technology: Mit opencourseware).

[7] John Hubbard. Electron correlations in narrow energy bands. In *Proceedings of the Royal Society of London A: Mathematical, Physical and Engineering Sciences*, volume 276, pages 238–257. The Royal Society, 1963.

[8] E Pavarini, E Koch, F Anders, and M Jarrell. Correlated electrons: from models to materials. *Reihe Modeling and Simulation*, 2, 2012.

[9] E Francisco and L Pueyo. Theoretical spin-orbit coupling constants for 3d ions in crystals. *Physical Review B*, 37(10):5278, 1988.

[10] LF Mattheiss. Electronic structure of ruo 2, oso 2, and iro 2. *Physical Review B*, 13(6):2433, 1976.

[11] BJ Kim, H Ohsumi, T Komesu, S Sakai, T Morita, H Takagi, and T Arima. Phase-sensitive observation of a spin-orbital mott state in sr2iro4. *Science*, 323(5919):1329–1332, 2009.

[12] Anatole Abragam and Brebis Bleaney. *Electron paramagnetic resonance of transition ions*. OUP Oxford, 2012.

[13] BJ Kim, Hosub Jin, SJ Moon, J-Y Kim, B-G Park, CS Leem, Jaejun Yu, TW Noh, C Kim, S-J Oh, et al. Novel j eff= 1/2 mott state induced by relativistic spin-orbit coupling in sr 2 iro 4. *Physical review letters*, 101(7):076402, 2008.

[14] MK Crawford, MA Subramanian, RL Harlow, JA Fernandez-Baca, ZR Wang, and DC Johnston. Structural and magnetic studies of sr 2 iro 4. *Physical Review B*, 49(13):9198, 1994.

[15] SJ Moon, Hosub Jin, WS Choi, JS Lee, SSA Seo, Jaejun Yu, G Cao, TW Noh, and YS Lee. Temperature dependence of the electronic structure of the j eff= 1 2 mott insulator sr 2 iro 4 studied by optical spectroscopy. *Physical Review B*, 80(19):195110, 2009.

[16] Mats Johnsson and Peter Lemmens. Crystallography and chemistry of perovskites. *Handbook of magnetism and advanced magnetic materials*, 2007.

[17] Farrel W Lytle. X-ray diffractometry of low-temperature phase transformations in strontium titanate. *Journal of Applied Physics*, 35(7):2212–2215, 1964.

[18] Feng Ye, Songxue Chi, Bryan C Chakoumakos, Jaime A Fernandez-Baca, Tongfei Qi, and Gang Cao. Magnetic and crystal structures of sr 2 iro 4: A neutron diffraction study. *Physical Review B*, 87(14):140406, 2013.

[19] S Boseggia, HC Walker, J Vale, R Springell, Z Feng, RS Perry, M Moretti Sala, Henrik M Rønnow, SP Collins, and Desmond Francis McMorrow. Locking of iridium magnetic moments to the correlated rotation of oxygen octahedra in sr2iro4 revealed by x-ray resonant scattering. *Journal of Physics: Condensed Matter*, 25(42):422202, 2013.

[20] Matthias Opel. Spintronic oxides grown by laser-mbe. *Journal of Physics D: Applied Physics*, 45(3):033001, 2011.

[21] Stephan Geprägs et al. *Magnetoelectric interactions in multiferroic thin films and composites*. PhD thesis, Technische Universität München, 2011.

[22] Antonio Miotello and Paolo M Ossi. *Laser-surface interactions for new materials production*. Springer, 2010.

[23] Matthias Opel, Stephan Geprägs, Matthias Althammer, Thomas Brenninger, and Rudolf Gross. Laser molecular beam epitaxy of zno thin films and heterostructures. *Journal of Physics D: Applied Physics*, 47(3):034002, 2013.

[24] Guus JHM Rijnders, Gertjan Koster, Dave HA Blank, and Horst Rogalla. In situ monitoring during pulsed laser deposition of complex oxides using reflection high energy electron diffraction under high oxygen pressure. *Applied physics letters*, 70(14):1888–1890, 1997.

[25] John David Jackson. *Classical electrodynamics*. Wiley, 1999.

[26] Albert Einstein. Zur elektrodynamik bewegter körper. *Annalen der physik*, 322(10):891–921, 1905.

[27] RP Walker. Interference effects in undulator and wiggler radiation sources. *Nuclear Instruments and Methods in Physics Research Section A: Accelerators, Spectrometers, Detectors and Associated Equipment*, 335(1):328–337, 1993.

[28] Primoz Rebernik Ribic and G Margaritondo. Status and prospects of x-ray free-electron lasers (x-fels): a simple presentation. *Journal of Physics D: Applied Physics*, 45(21):213001, 2012.

[29] SD Brown, L Bouchenoire, D Bowyer, J Kervin, D Laundy, MJ Longfield, D Mannix, DF Paul, A Stunault, P Thompson, et al. The xmas beamline at esrf: instrumental developments and high-resolution diffraction studies. *Journal of synchrotron radiation*, 8(6):1172–1181, 2001.

[30] Charles Kittel. *Introduction to solid state physics*. Wiley, 2005.

[31] William Henry Bragg and William Lawrence Bragg. The reflection of x-rays by crystals. *Proceedings of the Royal Society of London. Series A, Containing Papers of a Mathematical and Physical Character*, 88(605):428–438, 1913.

[32] G Van der Laan and BT Thole. Local probe for spin-orbit interaction. *Physical review letters*, 60(19):1977, 1988.

[33] BT Thole and G Van der Laan. Branching ratio in x-ray absorption spectroscopy. *Physical Review B*, 38(5):3158, 1988.

[34] BT Thole and G Van der Laan. Linear relation between x-ray absorption branching ratio and valence-band spin-orbit expectation value. *Physical Review A*, 38(4):1943, 1988.

[35] JP Hannon, GT Trammell, M Blume, and Doon Gibbs. X-ray resonance exchange scattering. *Physical review letters*, 61(10):1245, 1988.

[36] JP Hill and DF McMorrow. Resonant exchange scattering: polarization dependence and correlation function. *Acta Crystallographica Section A: Foundations of Crystallography*, 52(2):236–244, 1996.

[37] Luuk JP Ament, Michel van Veenendaal, Thomas P Devereaux, John P Hill, and Jeroen van den Brink. Resonant inelastic x-ray scattering studies of elementary excitations. *Reviews of Modern Physics*, 83(2):705, 2011.

[38] Björn Frietsch. *Magnetization Dynamics of Itinerant and Localized Electrons in Lanthanide Metals*. PhD thesis, Freie Universität Berlin, 2015.

[39] F De Bergevin and M Brunel. Observation of magnetic superlattice peaks by x-ray diffraction on an antiferromagnetic nio crystal. *Physics Letters A*, 39(2):141–142, 1972.

[40] F De Bergevin and M Brunel. Diffraction of x-rays by magnetic materials. i. general formulae and measurements on ferro-and ferrimagnetic compounds. *Acta Crystallographica Section A: Crystal Physics, Diffraction, Theoretical and General Crystallography*, 37(3):314–324, 1981.

[41] JG Vale, S Boseggia, HC Walker, R Springell, Z Feng, EC Hunter, RS Perry, D Prabhakaran, AT Boothroyd, SP Collins, et al. Importance of x y anisotropy in sr 2 iro 4 revealed by magnetic critical scattering experiments. *Physical Review B*, 92(2):020406, 2015.

[42] ST Bramwell, MJP Gingras, and PCW Holdsworth. Temperature dependence of xy-like order parameters in thin free-standing smectic liquid-crystal films. *Physical Review E*, 48(1):625, 1993.

[43] Malcolm F Collins. *Magnetic critical scattering*. Oxford University Press, 1989.

[44] Lars Onsager. Crystal statistics. i. a two-dimensional model with an order-disorder transition. *Physical Review*, 65(3-4):117, 1944.

[45] ST Bramwell and PCW Holdsworth. Magnetization and universal sub-critical behaviour in two-dimensional xy magnets. *Journal of Physics: Condensed Matter*, 5(4):L53, 1993.